2021-07-01

Design, synThesis, and optimization of additively manufactured functional ceramics and its composites

Anabel Renteria Marquez
University of Texas at El Paso

Recommended Citation

Renteria Marquez, Anabel, "Design, synThesis, and optimization of additively manufactured functional ceramics and its composites" (2021). *Open Access Theses & Dissertations*. 3328.
https://scholarworks.utep.edu/open_etd/3328

DESIGN, SYNTHESIS, AND OPTIMIZATION OF ADDITIVELY MANUFACTURED FUNCTIONAL CERAMICS AND ITS COMPOSITES

ANABEL RENTERIA MARQUEZ

Doctoral Program in Mechanical Engineering

APPROVED:

Tzu-Liang Tseng, Ph.D., Chair

Yirong Lin, Ph.D., Co-Chair

Alejandra Castellanos, Ph.D.

David Espalin, Ph.D.

Stephen L. Crites, Jr., Ph.D.
Dean of the Graduate School

Dedication

To my parents Lucia and Arturo, my sister, brother and friends

DESIGN, SYNTHESIS, AND OPTIMIZATION OF ADDITIVELY MANUFACTURED FUNCTIONAL CERAMICS AND ITS COMPOSITES

by

ANABEL RENTERIA MARQUEZ, M.S.

DISSERTATION

Presented to the Faculty of the Graduate School of
The University of Texas at El Paso
in Partial Fulfillment
of the Requirements
for the Degree of

DOCTOR OF PHILOSOPHY

Department of Mechanical Engineering
THE UNIVERSITY OF TEXAS AT EL PASO
August 2021

Acknowledgements

I would like to express my gratitude to my family for all their love and support during my journey of graduate school.

Secondly, I would like to express my gratitude to my committee chairs, Drs. Tzu-Liang Tseng and Yirong Lin for their guidance and economical support. Moreover, I would like to thank to my committee members Drs. David Espalin and Alejandra Castellanos for providing very insightful feedback that helped me to enrich my dissertation.

Lastly, I would like to thank to my research team Victor Balcorta, Aaron Rodriguez, Humberto Fernandez, and Jorge Diaz for their help and friendship over the years. My colleagues and friends Jaime Regis, Cory Marquez, and Samuel Hall for their contributions to help me improve my research.

Abstract

The goal of this research consist in the design, synthesis and optimization of functional piezoelectric ceramics and composites that can be fabricated by Direct Ink Write (DIW) 3D printing technique for the use of sensors and energy storage applications. The synthesis optimization of lead-free ceramics for printing was evaluated by analyzing the impact of raw particle size of $BaTiO_3$. A novel approach to evaluate the effect of bimodal distribution raw particle size of $BaTiO_3$ ceramics is presented and their influence on packing density, piezoelectric coefficient and dielectric relative permittivity. Additionally, multi-material DIW printing was adapted as a novel method to fabricate complete sensors in 'one-print' with better bonding. Such method was used for the fabrication of flexible PDMS- $BaTiO_3$ composites with PDMS-MWCNT electrodes.

Table of Contents

List of Tables

List of Figures

Chapter 1: Introduction

1.1 MOTIVATION

The motivation of this research goes to the design and optimization of functional materials using Additively-Manufacture techniques with no geometrical limitation and tunable mechanical properties. The growing demand in sensors, capacitors and actuators in recent years has led to an increased effort to improve materials proprieties of piezoelectric ceramics. However, the most of the piezoelectric ceramics have a high content of lead oxide, which could be dangerous for environment and the human being. For that reason, great efforts to improve materials properties of lead-free ceramics are needed. This dissertation aims to develop novel fabrication methods using Direct Ink Write 3D printing techniques with improved piezoelectric properties.

1.2 BACKGROUND

Functional ceramics are such materials that will activate a function as a reaction of an applied stimulus. Those types of materials have recently gained a lot of attention due to wide variety of applications for aerospace, industry and healthcare. Furthermore, piezoelectric materials are of particular interest due to the wide range of applications to fabricate embedded sensors, energy harvesters, vibration monitoring devices, sonar, pressure, and force sensors, among others.

Piezoelectric materials have the capability to generate an electrical output as a result of an applied mechanical stress also known as direct piezoelectric effect as shown in Figure 1.1. In a similar way, piezoelectric materials generate a mechanical strain as a result of an applied voltage which is known as converse piezoelectric effect.

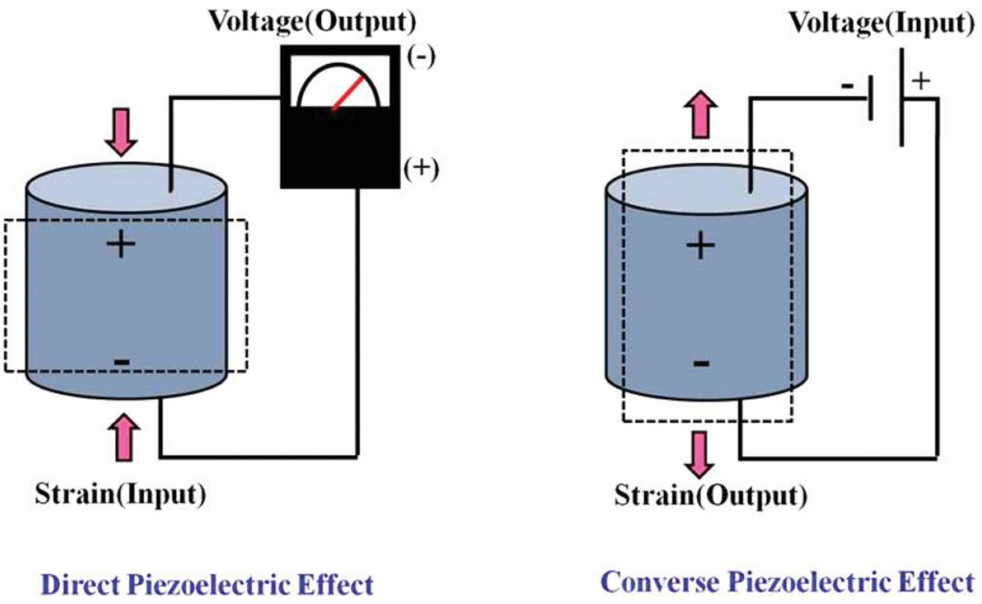

Direct Piezoelectric Effect

Converse Piezoelectric Effect

Figure 1.1: Direct and converse piezoelectric effect [1]

1.2.1 Piezoelectric ceramics

Among piezoelectric ceramics, lead magnesium niobite-lead titanate (PMN-PT) is the one known to have the best piezoelectric properties (d_{33}: ~2000 pC/N). Another well-known piezoelectric ceramic is lead oxide titanate ($Pb[ZrxTi1-x]O_3$ or PZT), which returns in high piezoelectric properties (d_{33}: ~500-600 pC/N), making it suitable for many industrial applications. However, there is a lot of concern regarding the damage that it could produce to the environment and the human being. Since PZT contains high levels of lead oxide (PbO), many researches opted to use and optimize lead-free materials, such as barium titanate ($BaTiO_3$) which is the lead-free ceramic with closest piezoelectric properties (d_{33}: ~190 pC/N) like PZT.

Lead-free ceramics

Barium titanate ($BaTiO_3$) is one of the most reported lead-free piezoelectric ceramics due to the wide variety of industrial and commercial applications that it can be used. Furthermore, $BaTiO_3$ offers material properties that makes it suitable for sensors, capacitors and energy harvesting devices $BaTiO_3$ is distinguished to have a good piezoelectric coefficient (d33: ~190 pC/N) [2] and high-dielectric permittivity (ε ~1700 at room temperature). A lattice of $BaTiO_3$ consists of eight Ba atoms at the corner, six O atoms at the planes and lastly, one Ti atom in the center as shown in Figure 1.2. $BaTiO_3$ has also four different material phases that are influence by the temperature. At room temperature, $BaTiO_3$ has a tetragonal structure, which is a ferroelectric state of the material. During poling process, a high voltage is applied to $BaTiO_3$, which drags the Ti atom to the direction of the applied field. This shift in the Ti atom produces a positively net charge and thus attracting negative charges, this effect on the dipoles moments is known as polarization. However, it is important to mention that this dipole moment will be lost if the Curie temperature is reach (T > 120 °C).

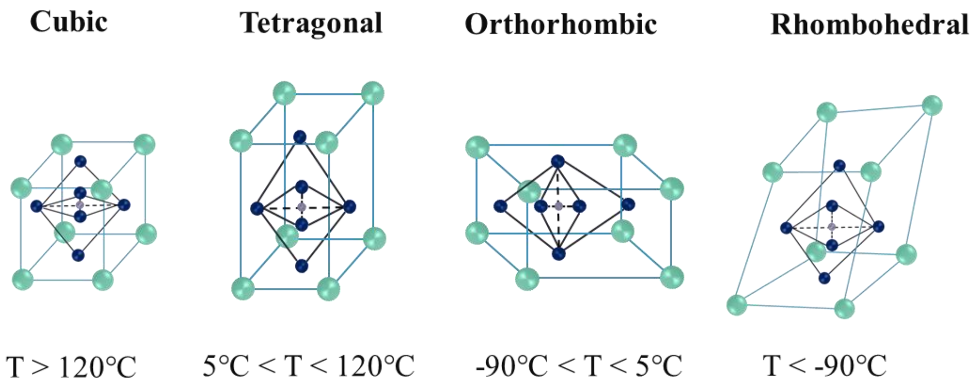

Figure 1.2: BaTiO3 different material phases at various temperature ranges

1.2.1 Additive Manufacturing

Additive manufacturing (AM) frequently referred as 3D printing, is a manufacturing technology commonly used for rapid prototyping to fabricate three-dimensional parts from a CAD design. The American Society for Testing and Materials (ASTM) group F42 divides AM on seven categories: vat photopolymerization (VP), powder bed fusion (PBF), material jetting (MJ), binder jetting (BJT), material extrusion (ME), sheet lamination (SL) and direct energy deposition (DED).

AM enables the possibility to expand ceramic fabrication through complicated design and low cost. Among the advantages of 3D printing are the possibility of using a wide variety of materials, high design complexity, and reduced fabrication time [1].

There are different available technologies that can be used in the fabrication of ceramics as illustrated in Figure 1.3. Different researchers have reported the use of PBF and BJT as an easy option to fabricate complex designs with a minimal feedstock preparation. However, the samples fabricated by this technology required the use of only micro particles and samples after sintering have ended up on low density (around 50-60 % Theoretical Density). In the other hand, VP technique offers the possibility to fabricate ceramics with high density (around 90 % T. D.) and high resolution. Nevertheless, there are still a lot of material limitations and the fabrication process is quite long. Lastly, ME techniques such as Direct Ink Write (DIW) allows the fabrication of high-density ceramics (around 80-90 % T. D.) with a large material selection. Where the current limitations include low resolution and geometrical design limitations due to the nature of the printing technology.

Figure 1.3: Ceramics additive manufacturing technology

Direct Ink Write Technique

DIW consists in the deposition of a slurry through a nozzle by a piston or pressure driven mechanism, which is then deposited onto a substrate. This printing technique offers a low cost and fast printing process commonly used for prototyping. The main advantage of DIW is that different printable slurries with wide molecular weights and large material selection could be used by controlling its rheological properties. DIW does not require a heating temperature to retain structural shape due to partial solidification of the material after deposition. However, it is required to have a good storage modulus (G') in order to enable 'self-support' of the material during the printing process. The main drawback of DIW is that samples usually require post-treatment to fully solidify, which include thermal curing or photopolymerization. If this post-treatment process is not performed with appropriate measurements, parts could develop different quality defects, such as voids, cracks or warping.

1.2.3 Dissertation overview

This dissertation is structured as follows. Chapter 2 starts by evaluating different raw particle size in the fabrication of BaTiO3 piezoelectric ceramics fabricated by DIW and their impact on density, piezoelectric and dielectric relative permittivity. Chapter 3 covers the optimization process to fabricate ceramics by DIW using Design of Experiments looking to maximize density, piezoelectric coefficient, dielectric relative permittivity and dimensional accuracy. Lastly, chapter 4 includes a mathematical model and experimentation to evaluate bimodal powder distribution in the fabrication of ceramics and its effect on packing density, piezoelectric and dielectric properties.

Chapter 2: Particle size influence on material properties of BaTiO3 ceramics fabricated using freeze-form extrusion 3D printing

This chapter describes a method to fabricate high-density bulk BaTiO3 piezoelectric ceramics suspensions using polyvinyl alcohol (PVA) in deionized water solution. PVA is a water-soluble and biodegradable polymer that presents an elastic structure at low temperatures. This elastic structure facilitates the extrusion process and improves shape retention of desired geometry due to shear-thinning behavior for DIW. Furthermore, the evaluation of different powder particle size in the ceramic suspensions needs to be evaluated. Literature suggests that grain size plays an important role on density and material properties of ceramics. Therefore, formulation of the suspension and powder particle size have an essential role to fabricate high-density ceramics. Here, three different BaTiO3 particle sizes were evaluated using the same binder content. Aiming to determinate the optimal results in terms of materials properties with respect to the theoretical values of pure BaTiO3. This study proves the feasibility of using DIW technique in the fabrication of excellent material property ferroelectric ceramics for sensing applications.

2.1 Introduction

Ferroelectric ceramics with piezoelectric properties are widely used in industry for sensors and actuators applications[2–4]. Lead oxide ceramics, such as lead zirconate titanate or PZT is widely used for electronic applications due to its good piezoelectric coefficient [4–6]. However, lead oxide is a toxic material that increase environmental pollution [5,6]. Therefore, the fabrication of lead-free ceramics with excellent piezoelectric properties is an area of research interest. Barium titanate (BaTiO3; BTO) is one of the most used lead-free ceramics due to its good piezoelectric (d33: ~ 190 pC/N) properties for building sensors, capacitors, and energy storage devices [6]. Nonetheless, the piezoelectric theoretical value of BaTiO3 is relatively low in comparison with the theoretical value of PZT (d33: ~ 500-600 pC/N) [7]. Many studies have been focus on improving the piezoelectric coefficient of BaTiO3. Huan et al. fabricated BaTiO3/PVB disks by traditional manufacturing to analyze the grain size influence on the piezoelectric property by evaluating different settings for a two-step sintering process. Results demonstrate that two-step sintering achieves a grain size of 1µm and a maximum piezoelectric coefficient of 519 pC/N [8]. Zhu et al. fabricated BiFeO3-BaTiO3 disks to evaluate the sintering effect on the piezoelectric property and grain growth, obtaining a high value of 208 pC/N [9]. However, the capacity to fabricate different designs by traditional manufacturing as described in [8,9] were limited to the mold's shape and size.

Additive manufacturing enables the fabrication of complex designs of ceramics at a relatively low cost [10]. Different additive manufacturing techniques, such as material extrusion, binder jetting, direct energy deposition and stereolithography have been reported in the fabrication of ceramics [11,12]. Many studies have been focusing on the fabrication of different geometries of piezoelectric ceramics using 3D printing techniques. Kim et al. fabricated BaTiO3/PVDF nanocomposites through fused deposition modeling technique achieving a piezoelectric response after thermal poling of d31 of 21x10-3 pC/N [13]. Gaytan et al. fabricated BaTiO3 samples using binder jetting 3D printing technique achieving a theoretical density of 65.2% and a piezoelectric coefficient of 74.1 pC/N [14]. Although different additive manufacturing techniques were used to fabricate piezoelectric ceramics with complex designs, the density and mechanical properties were relatively low compared with the theoretical values.

Freeze-form Extrusion Fabrication (FEF) is a free-forming technique of Additive Manufacturing. FEF consists in the extrusion of an aqueous paste through a nozzle, which is deposited in a layer-by-layer fashion at low temperature (i.e., freezing point of the paste). This paste extrusion technique has some advantages compared with other material extrusion methods. FEF is an inexpensive and fast printing method used for rapid prototyping process technology [15]. FEF also enables the fabrication of high-density ceramics with good shape retention and mechanical properties [16]. Huang et al. fabricated aluminum oxide (Al_2O_3) ceramics using freeze-form extrusion, resulting in high-density ceramics with an average of 90% of the theoretical value [17]. Li et al. fabricated complex structures of Al_2O_3 using Ceramic On Demand Extrusion (CODE) technique, achieving good dimensional accuracy after sintering (15-19% shrinkage) and high-density ceramics with 97.5% theoretical value [18]. Although this technique is widely used due to the return of good material property, there is still little work reported on the feasibility of printing ferroelectric ceramics.

2.2 Experimental details

2.2.1 Materials

Three different particle size of BaTiO3 powder (100 nm, 300 nm, and 500 nm; Inframat, Manchester, CT) were selected to evaluate the effect of the piezoelectric response of ceramics. Polyvinyl alcohol (PVA) powder (Mw~89,000-98,000; Sigma Aldrich, St. Louis, MO) was used as a binder for the paste fabrication.

2.2.2 Synthesis and fabrication

A PVA aqueous solution was prepared by dissolving 13 wt. % PVA powder in deionized water under a heavy stirring of 500 rpm. The PVA in water solution was let to dwell and stirred for 20 minutes to ensure homogenization. Then, the solution was placed on a hot plate at 90°C for 20 minutes. The heating process allowed a complete dissolution of PVA powder in aqueous solution. After that, 70 wt. % BaTiO3 powder (e.g., 100 nm, 300 nm, 500 nm) was added gram by gram to the PVA solution and mixed by hand using a glass rod until a homogenous paste was obtained. The BaTiO3 content in the slurry was determined by its capability to flow through the 1 mm nozzle without experience any clogging. The paste was gently deposited into a syringe tube (60 ml; Soft-Ject, Virginia Beach, VA). Figure 2.1 illustrates the paste preparation process. The final paste composition represents 28.5 vol. % of solid loadings, 7.4 vol. % of binder and 64.1vol. % of solvent. This is in good agreement with literature as researches reported solid loading contents of up to 30 vol. % of BaTiO3 for slurry fabrication [19]. After the paste preparation, the loaded syringe was placed in the fridge at 5 °C for 2 hours. The paste was aged at low temperature to activate the elastic structure of PVA [20], which helped to achieve a constant material flow rate due to an increase in the viscoelastic response [21]. Aging also contributes to an increase in the storage modulus (G'), which facilitated the layer-by-layer stacking of material [21]. The extrusion of paste in a cold environment improved shape retention of green bodies, and facilitated the stack of material to a higher number of layers and compiled different geometries.

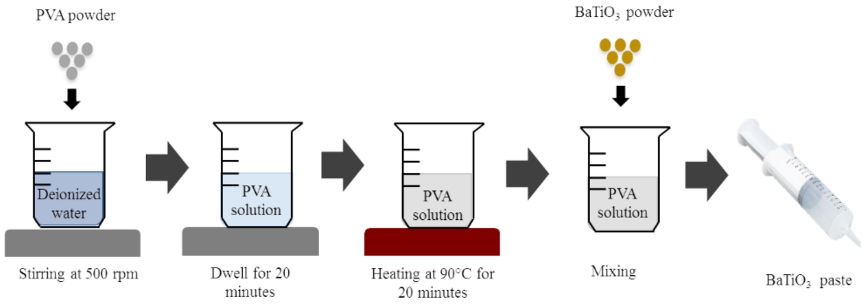

Figure 2.1: Schematic procedure for BTO/PVA aqueous paste.

2.2.3 Printing Process

Ceramic samples were printed in a modified Printrbot Simple Metal 3D printing machine. Figure 2.2 (a) describes the 3D printing structure, which consists of a piston that applies force over a plunger to extrude the material through a nozzle. A cylindrical geometry was selected to evaluate the particle size influence of BaTiO3. The dimensions of the sample were set to 25 mm for the outer diameter, 10 mm for the inner diameter and 13 mm height. The ceramic suspensions were deposited onto an aluminum froze plate at -40 °C, which was placed into the 3D printer substrate. The plate was covered with a thin film to facilitate the detach of green bodies after the printing process. Figure 2.2 (b) and (c) shows a cylinder and a square 3D printed structures respectively using FEF technique. Samples were printed using a nozzle diameter of 1 mm, with a speed of 10 mm/s, layer height of 0.6 mm and infill set to 80%.

After printing, the aluminum plate was removed from the printer bed and placed in the freezer at –60 °C (Thermo Scientific TSUTM Series -86 °C Upright Ultra-Low) for 2 hours to dry some of the water by sublimation to retain printed structural shape. Samples were detached from the aluminum plate, and it was found that the samples accumulated water on the bottom surface. To obtain homogeneous dried green bodies, the samples were turned upside down and placed back to the freezer for 30 minutes. A freeze-dried process contributes to shape retention and avoid warping of green bodies. After that, the samples were placed in the oven (Lab companion OF-01E) at 40 °C for 24 hours to remove any remaining water from the green body. Drying process at low temperatures for extended periods helps to avoid the generation of micro cracks in the green bodies [22,23].

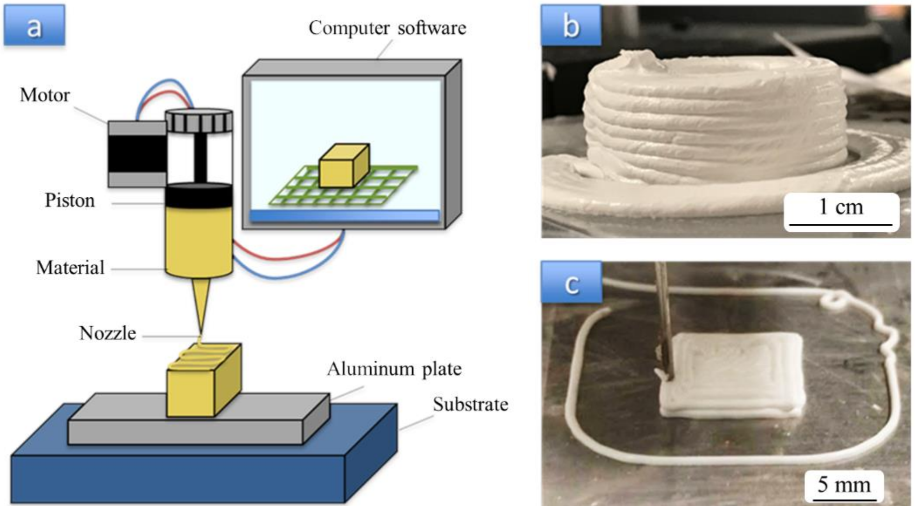

Figure 2.2: a) Structure of 3D printing machine used for paste extrusion b) 3D printed cylinder structure c) 3D printing process of a square structure

2.2.4 Post-Processing

To increase the density of the green bodies without causing any defect, such as external micro cracks, the sintering cycle of the samples were scheduled as follows. First, debinding to allow the PVA burnout followed by sintering of the sample to enable the grain size growth. All the samples were debinded at 600 °C for one hour and 5 °C/min ramp, then sintered at 1250 °C for two hours using 5 °C/min ramp. Lastly, samples were cool down at a 5 °C/min ramp to room temperature. After sintering, the samples were polished using 240-grit sandpaper to facilitate the dipole alignment poling process. Figure 2.3 shows two BaTiO3 ceramic samples, a green body after drying (left) and a sintered and polish sample (right). Conductive silver paint was applied on top and bottom surfaces and dried at 200 °C for 30 minutes. Thermal poling was performed under an electrical field of 5.4 kV/cm and submerged in silicon oil at 90 °C for two hours.

2.2.5 Material Characterization

Rheological properties of each BaTiO3-PVA suspension was measured in a DHR-2 rheometer (TA Instruments, New Castle, DE) with a parallel plate geometry. The gap between the plates was set to 1.2 mm, and the test was performed at 25 °C. The apparent density of the samples was measured by using the Archimedes' method. Then, compared with the theoretical value of pure BaTiO3 of 6.02 g/cm^3 [24]. The piezoelectric coefficient was calculated using a d_{33} meter (APC YE2730A). Dielectric permittivity was calculated using an LCR meter (1920 Precision, IET lab). The grain morphology characterization for different 3D printed BaTiO3 ceramics was observed by scanning electron microscope (SEM, TM-1000 Hitachi). Crystal structured was analyzed by x-ray diffraction (XRD) using CuKα radiation on a D8 discover diffractometer (Bruker).

Figure 2.3: BaTiO3 ceramic samples, green body (left) and sintered and polished (right).

2.3 Results and Discussions

2.3.1 Rheological Measurements

The slurry composition plays a critical role during the printing process, especially for shape retention and printability. The rheological properties of the slurry are highly influenced by the solid loadings content. Low solid loading contents produces a low viscous suspension, with a Newtonian behavior [25], which makes it unsuitable for printing. Low viscous slurries will tend to collapse as the number of layers of material increase [21]. In another hand, high solid loadings contents produces high viscous slurries with a high shear-thinning behavior [25]. High viscous suspensions restrict particle mobility, [25] increasing the probabilities of clogging during printing. Moreover, the shear stress over the walls of the nozzle will rise and higher yield strength will be required [21].

Figure 2.4 shows the results of viscosity as a function of shear rate for different BaTiO3-PVA suspensions varying powder particle size. A high influence on the rheological results was observed for different ink compositions. The ceramics suspensions index for a shear thinning behavior [21,26] since a reduction in viscosity was observed when increasing the applied shear rate. The shear thinning behavior can be attributed to the PVA content in the suspensions. PVA behaves as a non-Newtonian fluid and exhibits different viscoelastic properties depending on the concentration and molecular weight [26]. Additionally, a higher initial viscosity at low shear rates was observed for finer particles, which decreases at high shear rates. The stress profile under different shear rates is shown in Figure 2.5. It was found that a higher yield strength was required for finer particle size to rgenerate the initial flow through the nozzle. Once the flow is initialized, the yield strength required for printing stabilizes and remains in a constant range. The change in the yield strength to a constant phase can be attributed to a laminar flow behavior of the suspensions, which facilitate the deposition of material onto the substrate. Furthermore, literature indicates that particle size plays an important role in the rheology of the suspensions. Finer sizes increases the contact between the particles dispersed in the suspension increasing the viscosity [27]. The increase in viscosity can be attributed to liquid trapped inside aggregates of powder within the paste [28]. Moreover, finer particles are affected by Van der Waals forces, producing agglomerations in the slurries, which limits the matrix fluid [25]. In addition, the yield strength required to initialize the flow will increase, affecting the printing process.

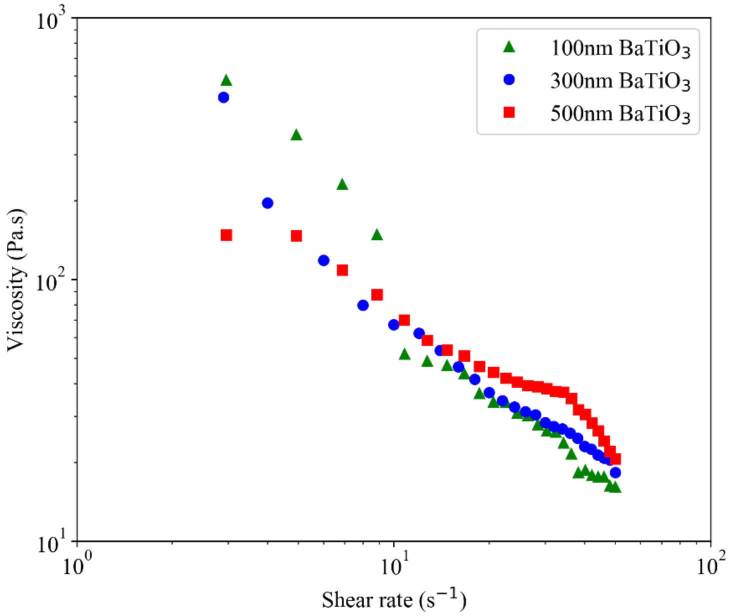

Figure 2.4: Evolution of viscosity as a function of shear rate for BaTiO3-PVA suspensions with 100 nm, 300 nm and 500 nm particle size.

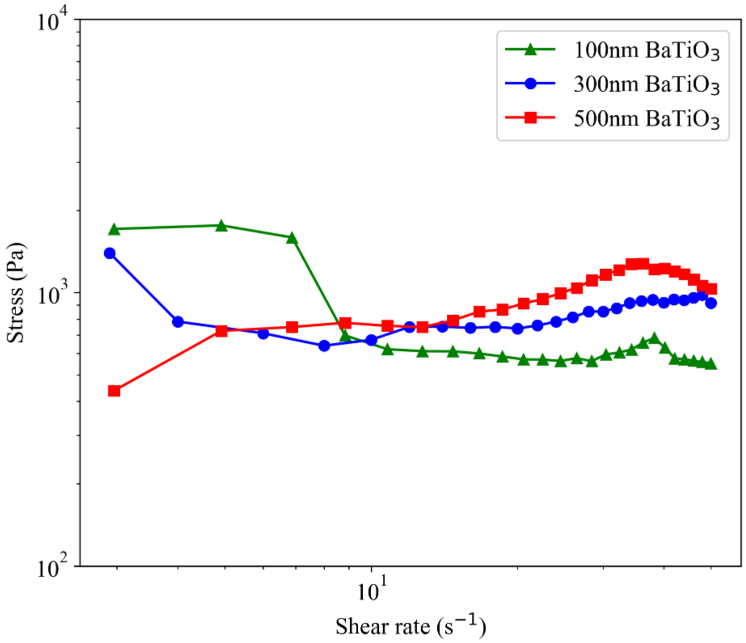

Figure 2.5: Stress behavior as a function of shear rate for BaTiO3-PVA suspensions with 100 nm, 300nm, and 500nm particle size.

2.3.2 SEM and XRD Analysis

The SEMs from the top surface and cross-section were observed to gain information about the microstructure and the porosity of the samples for different powder particles. The sintered samples were fractured to observe the microstructure from the cross-sectional area. Figure 2.6-A) presents a sample that was fabricated using 100 nm particle size. The average grain grow of ø≃ 1.18 μm was observed. Samples using 300 nm and 500 nm particle size are illustrated in Figure 2.6 B-C) respectively. An average grain size of ø≃ 0.871 μm for the 300 nm and ø≃ 0.757 μm for the 500 nm were observed. It was found that the average grain size after sintering decrease when increasing the powder particle size. Literature suggests that the final grain size after sintering is highly dependent of sintering temperature, exposure time and powder particle size [29]. Furthermore, reducing the powder particle size results in a higher curvature of the ceramic powder, meaning that a lower change in energy is required during sintering [30]. Figure 2.6-D:F) show the top surface for the 100 nm, 300 nm and 500 nm respectively. A reduction on the number of pores and pores sizes were observed when decreasing the powder particle size. The 100 nm sample showed a few voids ranging from 50 µm to 1 µm. However, the voids are not very deep as some grains can be observed inside the void. The 300 nm sample presents a more porous surface as voids of around 70 µm were observed. The 500 nm sample showed voids in the range of 25 µm to 5 µm at higher magnifications. However, the number of voids around the top surface were more than the 100 nm and 300 nm samples. The results obtained from the top surface complements the grain growth and porosity observed from the cross-sectional area. The reduction of pores for the 100 nm sample can be attributed to a higher rate of densification and a more uniform grain boundary.

The XRD for different BaTiO3 particle size are shown in Figure 2.7. The samples were evaluated in a range 2θ: from 20° to 80° at room temperature after poling process. The peaks observed in Figure 2.7-A index for tetragonal crystal structure [31]. The peaks splitting observed around at 2θ: 45 °, 51 °, 56 ° and 75 ° indicates a phase transformation from cubic structure. Furthermore, the peak splitting observed at (002) and (200) confirms the tetragonality phase of the samples, as shown in Figure 2.7-B. Phase transformation on BaTiO3 can be observed for heat treatments above 1000 °C. Moreover, BaTiO3 remains in the tetragonal crystal structure at room temperature, however the curie temperature at which it will transform to cubic is 120 °C [32]. The 100 nm sample showed a higher peak splitting intensity, which indicates a higher degree of crystallinity. These results are in good agreement with literature according to the following points. Several studies indicate that ferroelectric domain is influence by the size of the crystals [33], which can be controlled by the heat treatment temperature [8,32–34]. The BaTiO3 samples were exposed to the same treatment temperature of 1250 °C for the same period of time. The difference on degrees of crystallinity are attributed to the final grain growth obtained during the sintering process.

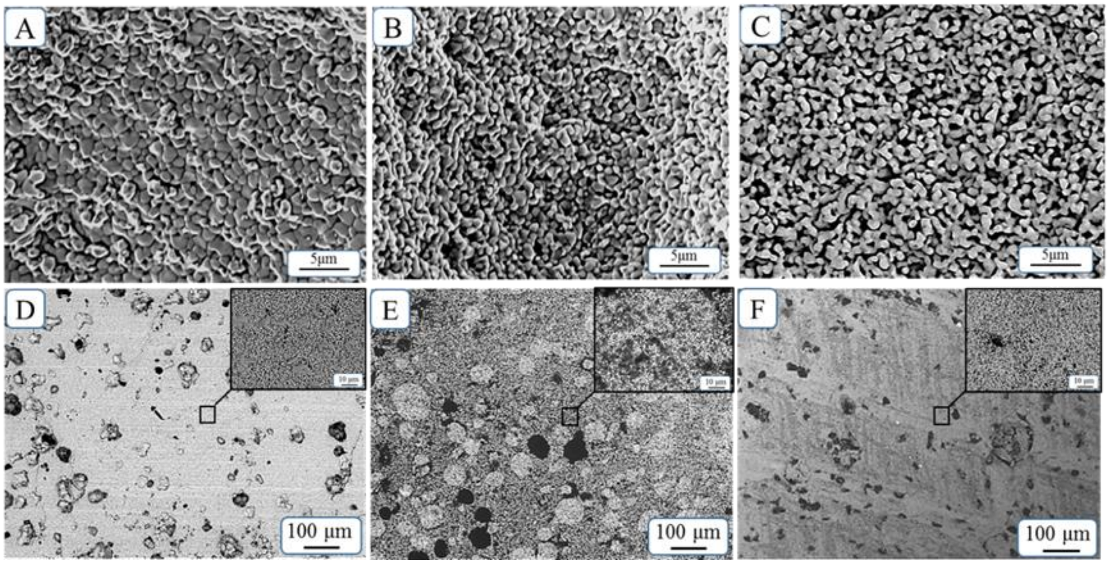

Figure 2.6: BaTiO3 samples after sintering at 1250°C. Cross-section for (A) 100 nm sample (B) 300 nm sample and (C) 500 nm sample. Top surface and surface microstructure for (D) 100 nm sample (E) 300 nm sample and (F) 500 nm samples

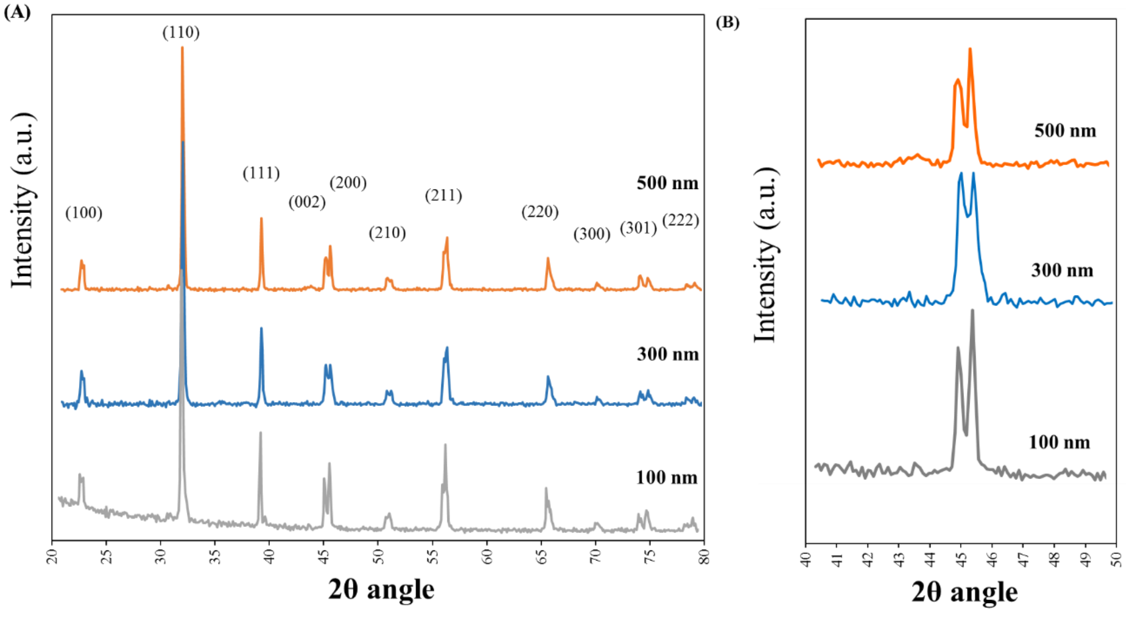

Figure 2.7: A) XRD for BaTiO3 for 100nm, 300nm and 500nm powder particle size in range 2θ: from 20° to 80°. B) XRD at peaks (002) and (200) in a range 2θ: from 40° to 50°.

2.3.3 Material Properties

Figure 2.8-A) shows the density results obtained for different particle size after sintering process. The relative densities for the 100 nm, 300 nm and 500 nm were 5.13 ± .35 g/cm3, 4.35 ± .32 g/cm3 and 4.09 ± .42 g/cm3 respectively; which correspond to 85.24% ± 5.74%, 72.19% ± 5.27% and 67.94% ± 6.91% of the theoretical value for pure BaTiO3. It was found that the relative density after sintering increased when reducing the powder particle size. This is in good agreement with the grain-growth observed from the SEMs microstructure. Coarse powder particles showed a lower increase in the final grain-growth, which increase the number of voids on the samples. Additionally a higher level of porosity can led to lower material properties. The piezoelectric coefficient results are presented in Figure 2.8-B). A positive increment on the d33 was observed for finer powder particles. The piezoelectric coefficient (d33) were 204.61 ± 16.87 pC/N, 127.63 ± 8.19 pC/N and 112.2 ± 7.99 pC/N for the 100 nm, 300 nm and 500 nm respectively; which correspond to 107.12% ± 8.83, 66.82% ± 4.29 and 58.74% ± 4.18 of the theoretical value of 191 pC/N [24]. The increment on the piezoelectric coefficient can be attributed to the higher grain growth at the micron level when using finer particles [24,33,34]. Different studies suggest that there is a strong dependency in the grain size and the piezoelectric properties [24]. Furthermore, BaTiO3 crystalline structure is influenced by the domain walls width, which contributes to the piezoelectric response. Grain size in the micron level decrease the 90° domain width, producing a smaller domain walls [8]. The decrease in the domain walls facilitate its rotation, which increase the sensibility to an external stress or electrical signal [8]. Figure 2.8-C) shows the dielectric permittivity (ε) results, the measurements were performed at 25 °C with a frequency of 1 kHz. The dielectric permittivity obtained for the 100 nm, 300 nm, and 500 nm, which were 2250 ± 270, 1636.34 ± 199.7 and 1333.07 ± 157 respectively. These values correspond to 115.38% ± 13.84, 83.89% ± 10.24 and 68.35% ± 8.05 of the theoretical value of BaTiO3 of 1950 at 90 °C [34]. Different studies suggest that the dielectric constant increase when the grain growth is at the

micron level [35,36]. Additionally, a uniform grain-size distribution is required to achieve a higher permittivity [37,38]. Furthermore, residuals of binder content of the sample may influence the dielectric permittivity results. Literature suggest that impurities such as carbon residues may be encapsulated inside the sample increasing the permittivity [39,40]. Finer particles reached higher density with a significant lower number of voids, reducing the space in the grain boundaries, preventing the escape of carbon from the sample during sintering increasing the permittivity.

The results obtained for density and material properties are comparable with previous studies that report the fabrication of piezoelectric ceramics using Additive Manufacturing. For robocasting, ref. [4] reported a density of 65.3%, a piezoelectric coefficient of 200 pC/N and a dielectric permittivity of 4730 at 1 KHz for BaTiO3. In the fabrication of PZT composites a piezoelectric coefficient of 300 pC/N and dielectric permittivity if 2250 at 10 kHz [13]. In another hand, for binder jetting, ref. [14] a density of 65.2%, a piezoelectric of 74 pC/N and a dielectric permittivity of at 1 kHz for $BaTiO_3$ were reported. This study contributes with a fabrication method for $BaTiO_3$ ceramics with higher density and similar material properties as previous published works. Proving the feasibility of the slurry composition and FEF technique.

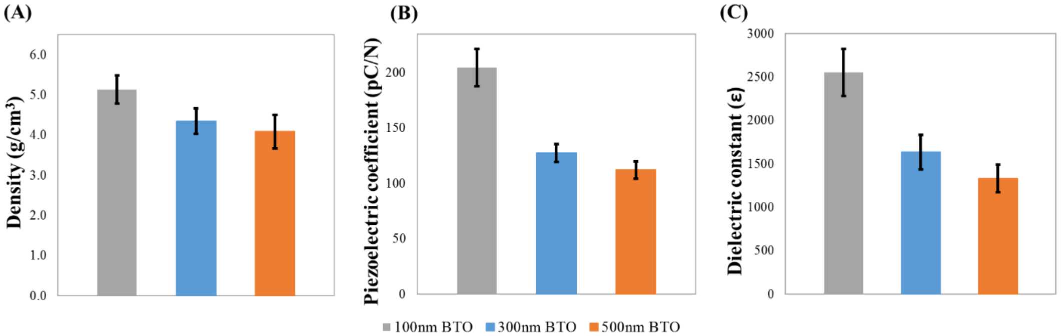

Figure 2.8: Average result of density, piezoelectric coefficient and dielectric constant

2.4 Conclusion

A simple method to fabricate high-density BaTiO3 ceramics using freeze-form extrusion fabrication (FEF) was presented. Three different particle size of BaTiO3 were investigated in terms of their influence on density, piezoelectric coefficient, and dielectric permittivity. Results showed that finer BaTiO3 particles could lead to better material property due to a higher grain growth after sintering. Using 100 nm particle size, a density of 5.13 ± .35 g/cm3 can be achieved, which correspond to 85.24% ± 5.74 of the theoretical value. A high piezoelectric coefficient (d33) of 204.61 ± 16.87 pC/N was obtained, corresponding to 107.12 % ± 8.83 of the theoretical value of 191 pC/N. A dielectric constant of 2551.09 ± 270 at 1 kHz was obtained, representing 115.38 % ± 13.84 of the theoretical of 1950. The grain size and morphology was observed through SEM, which corroborated the experimental results on density, piezoelectric and dielectric. XRD analysis confirmed the tetragonal crystal structure in the samples after sintering. These results demonstrated the feasibility of using FEF technique as an inexpensive method for rapid prototyping design of bulk piezoelectric devices such as sensors and actuators with the possibility of a high degree of customization and excellent material properties.

Chapter 3: Optimization of 3D Printing Parameters for BaTiO3 Piezoelectric Ceramics through Design of Experiments

Paste extrusion is an additive manufacturing technique that deposits paste through a nozzle in a layer-by-layer fashion to form a three-dimensional object. This technique can be used to fabricate piezoelectric ceramics with complex geometries and excellent material properties to fabricate sensors, capacitors, and energy storage devices with a high level of customization. Different factors can affect the quality of piezoelectric ceramics when using the paste extrusion technique, for example, the composition of the paste and printing parameters. This chapter presents a study to optimize the piezoelectric coefficient, relative density, dielectric permittivity and dimensional accuracy of BaTiO3 by using design of experiments with a 2^{k-1} design. Results indicated that the factors having a significant impact on the end-product outputs were the BaTiO3 particle size and the binder concentration on the paste formulation. Using the optimal levels makes it possible to achieve a piezoelectric coefficient higher than 200 pC/N and a density of 90 % of the theoretical value of pure BaTiO3.

3.1 Introduction

Additive Manufacturing (a.k.a. 3D Printing) consists of the deposition of material in a layer-by-layer fashion to form a three-dimensional object. This technique is widely used for rapid prototyping, especially when the fabrication of complex geometries is required. Materials including metals, polymers, and ceramics are used for additive manufacturing processes [41]. Literature reports efforts in the fabrication of ceramics using different additive manufacturing techniques such as material jetting, material extrusion, direct energy deposition, binder jetting and stereolithography [11,12]. The fabrication of ceramics is an area of interest due to their excellent thermal, mechanical, and electric properties, which are useful in several applications in the area of electronics and beyond [42,43]. However, ceramics fabricated using additive manufacturing are hard to process because they must be sintered to remove the binder content to obtain a densified sample [12]. This debinding process can lead to nonconforming samples with high levels of porosity especially for powder-based methods, or inhomogeneity causing cracks and reducing the mechanical strength of the final product for slurry-based methods. For this reason, the fabrication of ceramics with designed complex geometries and defects-free becomes a challenge.

Many research studies have been reported on the fabrication of technical or functional ceramic objects using free-forming techniques. Freeze-form Extrusion Fabrication (FEF), Ceramic Extrusion On Demand (CODE) and Robocasting are some examples of this technique. For technical ceramics, researches commonly reported the use of Alumina (Al2O3) [12,44], Silica (SiO2) and Silicon Nitrate (Si3N4) [45]. For example, Huang et al. used FEF to fabricate complex geometries with Al2O3 achieving a density of 90% with respect to the theoretical value [17]. For functional ceramics, researchers reported studies using ferroelectric ceramics [4] and magnetic ferrite ceramics [46]. Ferroelectric ceramics are specifically of interest due to their piezoelectric properties. Piezoelectricity refers to the generations of an electric signal when mechanical loads are applied or vice versa [47]. Pb(ZrxTi1-x)O3 or PZT is a ferroelectric ceramic known to have good piezoelectric properties (d33~500-600 pC/N) [47], and it is widely used for sensors and capacitors applications [3]. However, the use of toxic materials such as lead oxide (PbO), especially for electronic devices could increase the environmental pollution and harm the human body [6]. From Barium Titanate (BaTiO3 or BTO), is known to have good piezoelectric properties (d33~190 pC/N) and can be used as sensors and capacitors with comparable properties to PZT.

Although Additive Manufacturing enables the fabrication of ceramics with complicated design, the optimization of the fabrication process is still required. Design of Experiments (DOE) is a statistical tool that evaluates different factors and their impact in the end-product output. DOE also allows to determine the optimal level of these factors to maximize the desired output. Several authors have used statistical analysis to optimize the fabrication process for different additive manufacturing techniques [48–50]. For example, Chen and Zhao investigated the process parameters that influence the surface quality of stainless steel powder manufactured with Binder Jetting technique using Signal to Noise ratio and ANOVA analysis. The factors considered in this study were layer thickness, printing saturation, heater powder ratio and drying time. They demonstrated that layer thickness was the most significant factor affecting surface roughness. The drying process showed the highest impact on the shrinkage of the samples [6]. Yan et al. investigated the factors that affect the liquid phase migration of Al2O3 fabricated with FEF. The factors studied were extrusion velocity, extrusion interval time and nozzle length and analyzed with an orthogonal design of experiments. It was found that extrusion velocity and extrusion interval time have an impact on the liquid phase migration of FEF [51].

Even though a considerable amount of research has been dedicated to the optimization of ceramics, there is insufficient work reported on functional ceramics such as piezoelectrics. To obtain high-quality ceramics, techniques such as FEF have been developed to increase density and piezoelectric properties. FEF is an additive manufacturing technique that extrudes and deposits paste through a nozzle onto a substrate below the freezing temperature of the paste. This free-forming technique is an inexpensive slurry-based method that can fabricate complex designs of ceramics with better shape retention and high density. This chapter aims to optimize the fabrication of BaTiO3 ferroelectric ceramics using FEF technique through DOE with a fractional factorial 2k-1 design. This study considers the evaluation of four different factors: particle size, binder amount, nozzle diameter, and printing speed.

3.2 Experimental details

3.2.1 Materials

BaTiO3 powder supplied from Inframat (Manchester, CT) was selected as solid loading of the paste. Polyvinyl Alcohol (PVA) powder (Mw~ 89,000-98,000) supplied from Sigma Aldrich (St. Louis, MO) was determined to be the binder in the ceramic suspensions. For the paste preparation, PVA powder was dissolved in deionized water using a stirring rate of 500 rpm and let to dwell for 20 minutes. Then, the solution was placed in a hot plate at 90 °C for 20 minutes to achieve a homogeneous dispersion of the PVA powder. After that, BaTiO3 powder was added to the solution and mixed until a homogenous paste was obtained. All the ceramics suspensions were fabricated using 70 wt. % BaTiO3 and 30 wt. % PVA solution. Lastly, the paste was deposited into a syringe tube and sealed immediately to prevent water evaporation.

3.2.2 Factors and Levels

A two-level fractional factorial design 2k-1 was selected to optimize the fabrication of BaTiO3 ferroelectric ceramics. This statistical design considers the evaluation of k factors with two levels of interest. However, when a large number of factors are evaluated, it is recommended that a k-1 design is used, as the number of runs per replications could overcome available resources. Table 3.1 refers to the factors and levels considered for this study. BaTiO3 particle size was selected as a factor, using 300 nm as high level and 100 nm as low level. The particle size of BaTiO3 is a factor of interest as it may influence the mechanical properties of the final product. The PVA concentration was also selected, since the binder content may affect the rheology of the ceramic suspensions. The high level of PVA was set to 13 wt. % in deionized water, and the low level was set to 9 wt. % in deionized water. Another factor was printing speed; since different flow-rates can affect the relative density and the dimensional accuracy of the green bodies. The high and low level for printing speed was set to 20 mm/s and 10 mm/s respectively. The last factor selected was the nozzle diameter; the high level was set to 1.2 mm while the low level was set to 0.8 mm. The nozzle diameter can possibly affect the dimensional accuracy of the green bodies due to the shear stress generated in the walls of the nozzle and the stress required for the piston of the machine to achieve a constant flow [20]. The fractional factorial design 2^{k-1} was created with Minitab using the information provided in Table 3.1. This study considers three replications and a randomized order to validate the results. Table 3.2 shows an example of the runs required, considering all the different runs for one replication.

Table 3.1: Factors and levels for design of experiments.

	Levels	
Factors	*Low*	*High*
PVA in deionized water	9 wt%	13 wt%
BTO particle size	100 nm	300 nm
Printing speed	10 mm/s	20 mm/s
Nozzle diameter	0.8 mm	1.2 mm

Table 3.2: Runs per replication

Run	PVA in deionized water (wt%)	BTO particle size (nm)	Printing speed (mm/s)	Nozzle diameter (mm)
1	9	100	10	0.8
2	9	100	20	1.6
3	9	300	20	0.8
4	9	300	10	1.6
5	13	100	20	0.8
6	13	100	10	1.6
7	13	300	10	0.8
8	13	300	20	1.6

3.2.3 Fabrication Process

The samples were printed using a Printrbot Simple Metal 3D printing machine, which was modified to extrude paste. A cylinder of 1-inch outer diameter, ½-inch inner diameter, and ½-inch height was selected as the standard sample for this study. Figure 3.1-A) shows the CAD design of the cylinder in Slic3r software. The printing process of the samples follows a randomized order. Additionally, the samples were identified immediately with the run number according to the DOE table as illustrated in Figure 3.2. During the printing, an aluminum freezing plate was placed onto the substrate at -40 °C. The plate was covered with a thin film to allow for an easier detachment of the samples. After printing, the aluminum plate was removed from the bed and placed in a freezer at -60 °C (Thermo Scientific TSUTM Series -86 °C Upright Ultra-Low) for 12 hours to dry some of the water content by sublimation. To prevent the generation of cracks, the samples were placed upside down in the freezer for another 30 minutes. The samples were also dried in an electric oven (Lab companion OF-01E) at 40 °C for 24 hours to remove any remaining water from the green body. A slow drying process under low temperatures prevents the generation of microcracks in the green bodies [52]. Figure 3.1-B) shows an example of an as-printed BaTiO3 sample. The angle after drying was measured, comparing the displacement of the last printed layer with respect to the first layer as shown in Figure 3.8 .Some of the samples presented an inferior ability to stack the material during the printing process. This issue was observed mainly on the pastes that contained a higher water content level. The density of the green bodies was measured using Archimedes' principle and compared with the theoretical density of BaTiO3 of 6.02 g/cm3 [53] (Table 3.3). The density of the green bodies was 1.67 g/cm3 on average before sintering. This relatively low-density value is attributed to the amount of water and binder content in the as-printed samples.

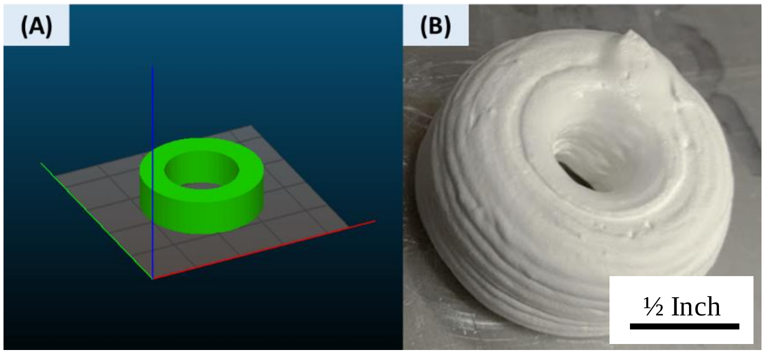

Figure 3.1: A) Cylinder design on Slic3r B) BaTiO3 green body 'as-printed.'

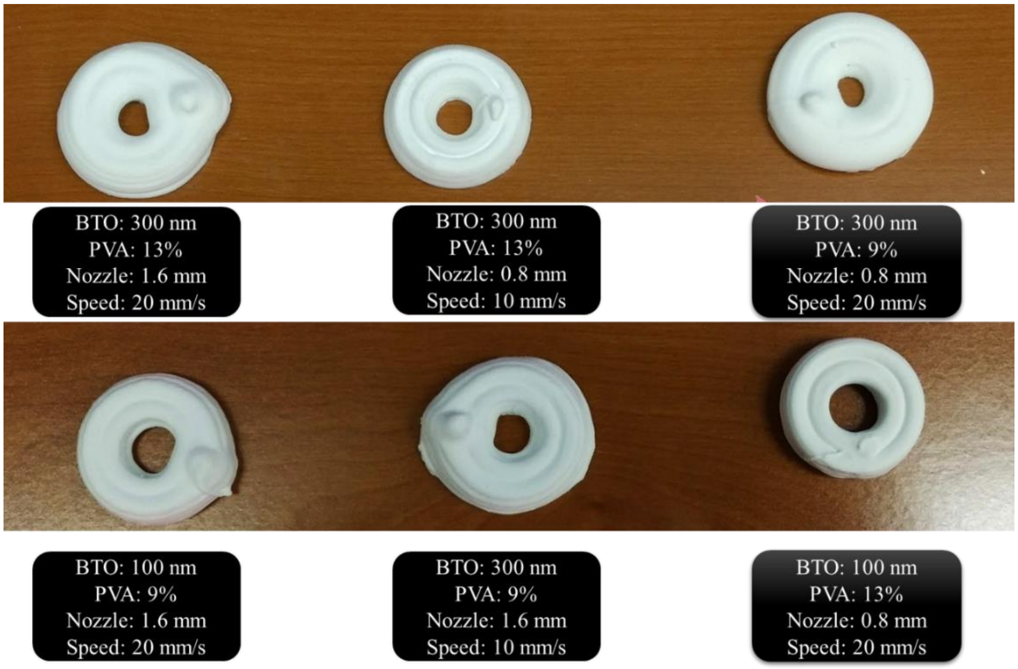

Figure 3.2: Samples replications of dried green bodies of BaTiO3-PVA ceramics.

3.2.4 Post-Processing

The samples were printed All the samples were debinded at 600 °C for one hour and sintered at 1250°C for two hours at 5°C/min ramp. After sintering, the samples were polished using sandpaper 240-grit. Conductive silver paint was applied in the top surface, then dried at 400 °C for 15 minutes. The same process was repeated for the bottom surface of the samples. Each sample was exposed to thermal poling on silicon oil for 2 hours for dipoles alignment. The electrical field and the temperature were set to 5.4 kV/cm and 90 °C respectively. The piezoelectric coefficient was calculated using a d33 meter (APC YE2730A). Dielectric permittivity was calculated with an LCR meter (1920 Precision, IET lab).

3.2.3 Material Characterization

The grain morphology characterization of the samples after sintering was observed using a scanning electron microscope (SEM, TM-1000 Hitachi). Figure 3.4-A) shows the cross-section of a 300 nm BaTiO3 and 9 wt. % PVA sample after sintering. The density for this sample was 4.03 g/cm3, which represents 66.95 % of the theoretical value. It was also observed that the grain size was ø ≃ 1 µm on average. Figure 3.4-B) presents the cross-section of a 100 nm BaTiO3 and 13 wt. % PVA sample after sintering. The density for this sample was 5.22 g/cm3, which represents 86.75 % of the theoretical value. The 100 nm BaTiO3 sample showed bigger grain sizes of ø ≃ 3 µm on average. There is an evident increase in density for finer particle sizes. Researchers suggest that finer particle size tends to achieve a higher grain growth due to high curvature of the ceramic powder, which requires a lower change in energy during sintering.

Crystal structure of the samples was analyzed by x-ray diffraction (XRD) on a D8 discover diffractometer (Brucker). Figure 3.3 shows the XRD for 100 nm and 300 nm BaTiO3 particle size after sintering using a range 2θ from 20° to 80°. The peaks splitting at (002) and (200) for both particle size index for a tetragonal crystal structure [54]. Previous studies report that a transition from cubic to tetragonal phase can be observed in BaTiO3 using heat treatments above 1000°C [21]. A higher peaks intensity at (002) and (200) was observed for the 100 nm BaTiO3 sample, which can be attributed to a higher grain growth after sintering. Researchers reported that the growth of BaTiO3 crystallite strongly depend on the heat temperature and exposure time during the sintering process.

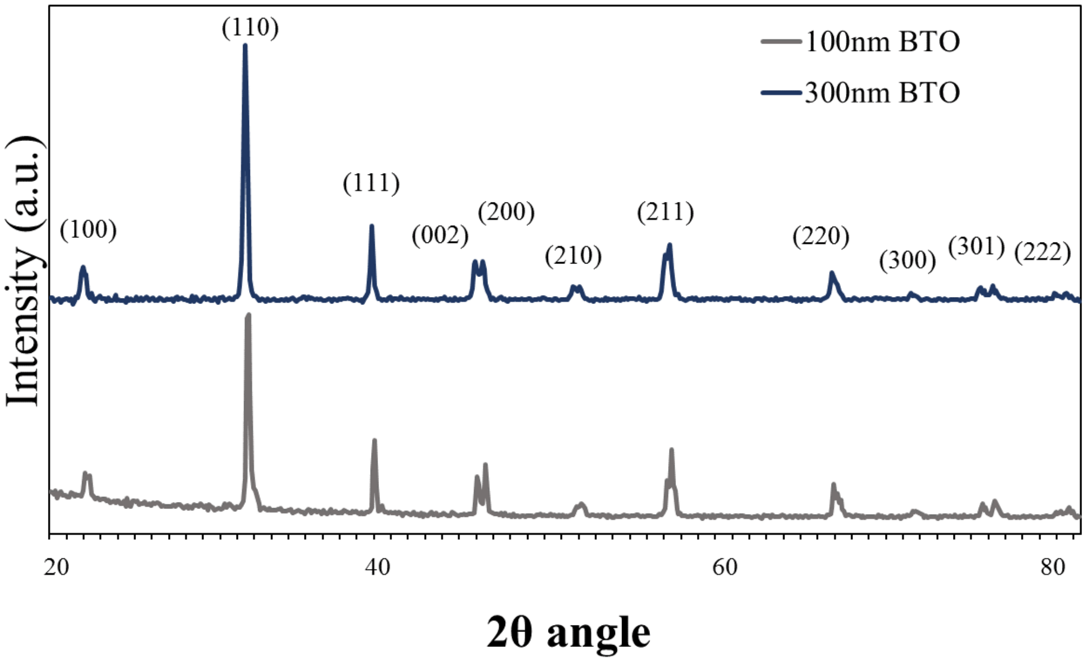

Figure 3.3: XRD of 100nm and 300 nm BaTiO3 particle size in range 2θ from 20° to 80°.

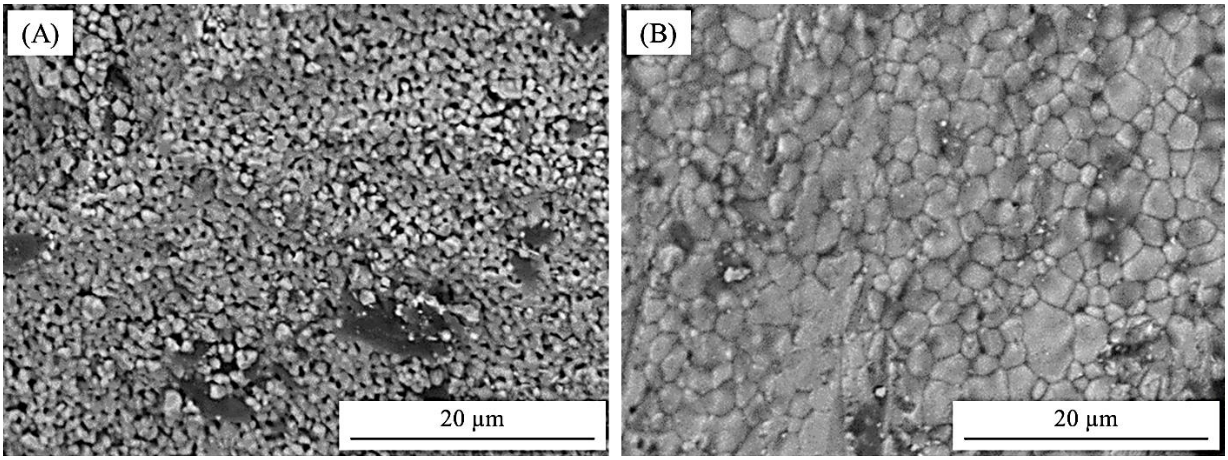

Figure 3.4: A) Cross section of a 300 nm BaTiO3 9 wt. % PVA sample after sintering B) Cross section of a 100 nm BaTiO3 13 wt. % PVA sample after sintering.

3.3 Results and Discussions

3.3.1 Rheological Measurements

The factors and levels selected in Table 3.1 are justified with the rheology characterization of the paste formulation. Proper rheology can guarantee a constant flow and printability of the samples [20]. All the different pastes were measured in a DHR-2 rheometer (TA Instruments, New Castle, DE) at room temperature, using a parallel geometry with a 1.2 mm gap. Figure 3.5 A) shows the viscosity of each ceramic suspension as a function of shear rate in the ranges of 1 to 50 s-1; while Figure 3.5 B) shows a magnified version of the viscosity in a shear rate of 10 to 30 s-1. Figure 2 shows the stress profile at different shear rates in the ranges of 1 to 50 s-1. All the ceramic suspensions presented a shear thinning behavior [55,56] as low shear rates require higher force due to the initial viscosity of the paste. However, high shear rates require lower applied force. The initial high force is required to generate the flow through the nozzle. Also known as the dynamic yield stress of the fluid. It was found that the suspensions with higher PVA concentration had a higher viscosity and thus required more initial force applied. Furthermore, it was observed that finer particle size of BaTiO3 also affects the viscosity. The rheology of the different ceramic suspensions is in good agreement with literature according to the following. PVA behaves as a non-Newtonian fluid in aqueous solutions and exhibits different viscoelastic properties depending on the concentration [25,55]. The increment on the viscoelastic properties observed can be attribute to a stronger hydrogen-bonding interaction of PVA when increasing its content [25,55]. Literature suggest that particle size also affects the rheology of the suspensions. Finer size could increase the contact between particles dispersed in the suspension affecting the viscosity [27]. The increase in viscosity can be attributed to liquid trapped inside aggregates of powder within the paste [57]. Figure 3.6 shows the printability zone at shear rates of 30 to 50 s-1 with ranges in viscosity between 40 to 10 Pa.s. Different viscosity values will affect the flow rate of the suspension during the fabrication of the samples and needs to be evaluated.

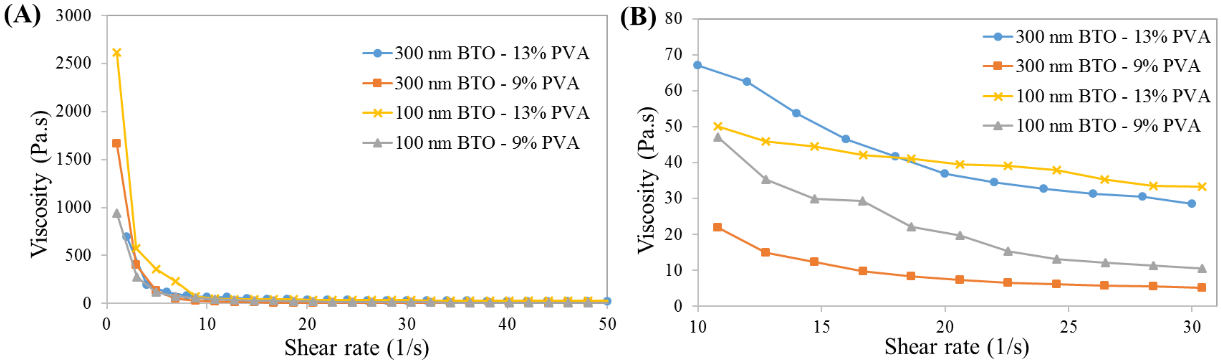

Figure 3.5: Viscosity profile as a function of shear rate for each BTO-PVA ceramic suspension A) shear rate in the ranges of 1 to 50 s-1 B) Magnification of viscosity in a shear rate range of 10 to 30 s-1.

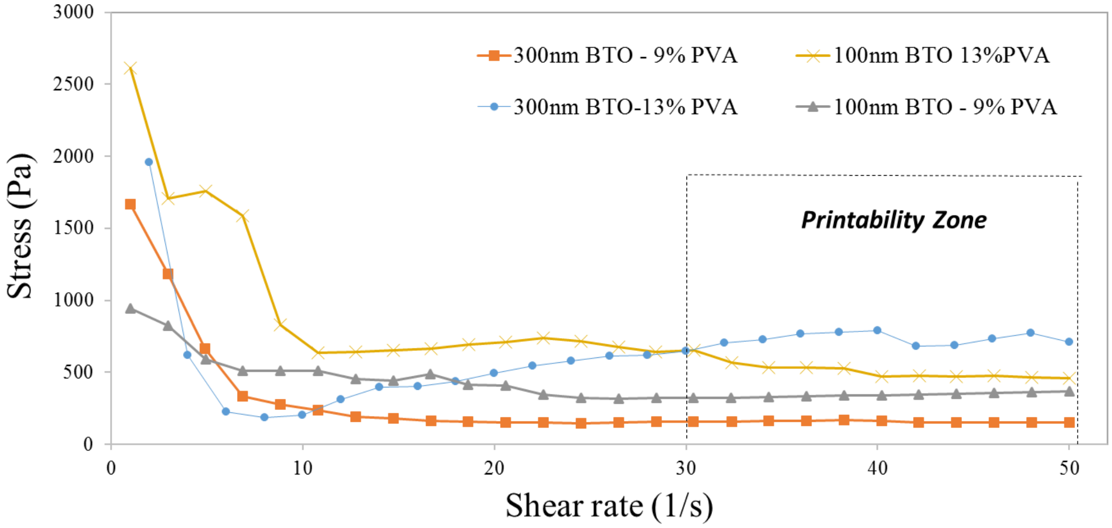

Figure 3.6: Stress behavior as a function of shear rate for each BTO-PVA ceramic suspension.

3.3.2 Statistical Results

This study considered the piezoelectric coefficient, dielectric permittivity, density, and dimensional accuracy as critical outputs to fabricate BaTiO3 ferroelectric ceramics. All the experimental results were collected (Table 3.4 to 3.7) and analyzed in Minitab. The normal probability plots of the standardized effect provided in Figure 3.7 presents the factors that have a statistical significance with respect to every individual output at a 95% confidence level. The interaction plot shown in Figure 3.9 to Figure 3.10 evaluates the effect of two variables and their impact on the end-output at a 95 % confidence level. Lastly, the main effect plots shown in Figure 3.9 presents an analysis of factors and levels that maximize every output.

For the piezoelectric response shown in Figure 3.7-A) the only significant factor was the BaTiO3 particle size. Figure 3.9-A) indicates that the 100 nm particle size is the level that will maximize the piezoelectric coefficient of the samples. This result is a good agreement with literature, which indicates that an increase on piezoelectric properties is observed when decreasing particle size of BaTiO3 [8,38,39]. Figure 3.7-B) indicates that the factors affecting the dielectric permittivity were the PVA concentration and the interaction (Figure 3.10) of PVA and BaTiO3. Figure 8-B) shows that 13 wt. % PVA is the level that will increase the dielectric permittivity. Results in the interaction plot indicate that the combination of PVA and BaTiO3 that maximize the output is 100 nm BaTiO3 and 13 wt. % PVA concentration. PVA is a carbon base binder, and although PVA was burnout during sintering, literature indicates that carbon residues may be encapsulated affecting the permittivity of ceramics [31,37]. Figure 3.7-C) shows that the only significant factor that has an impact on the density was the BaTiO3 particle size. Figure 3.9-C) shows that the 100 nm BaTiO3 particle size will achieve a higher density. The influence of the ceramic particle size is consistent with previous studies [58] suggesting that finer particle size normally achieve a higher grain growth due to high curvature of the powder. For dimensional accuracy, it was found that the PVA concentration was the only significant factor as shown in Figure 3.7-D). Figure 3.9-D) indicates that 13 wt. % PVA is the level that minimizes the angle of deformation and enables a better stack of material. This result is in good agreement with the rheology of the paste, which indicates that there is an increase in viscosity for higher binder contents.

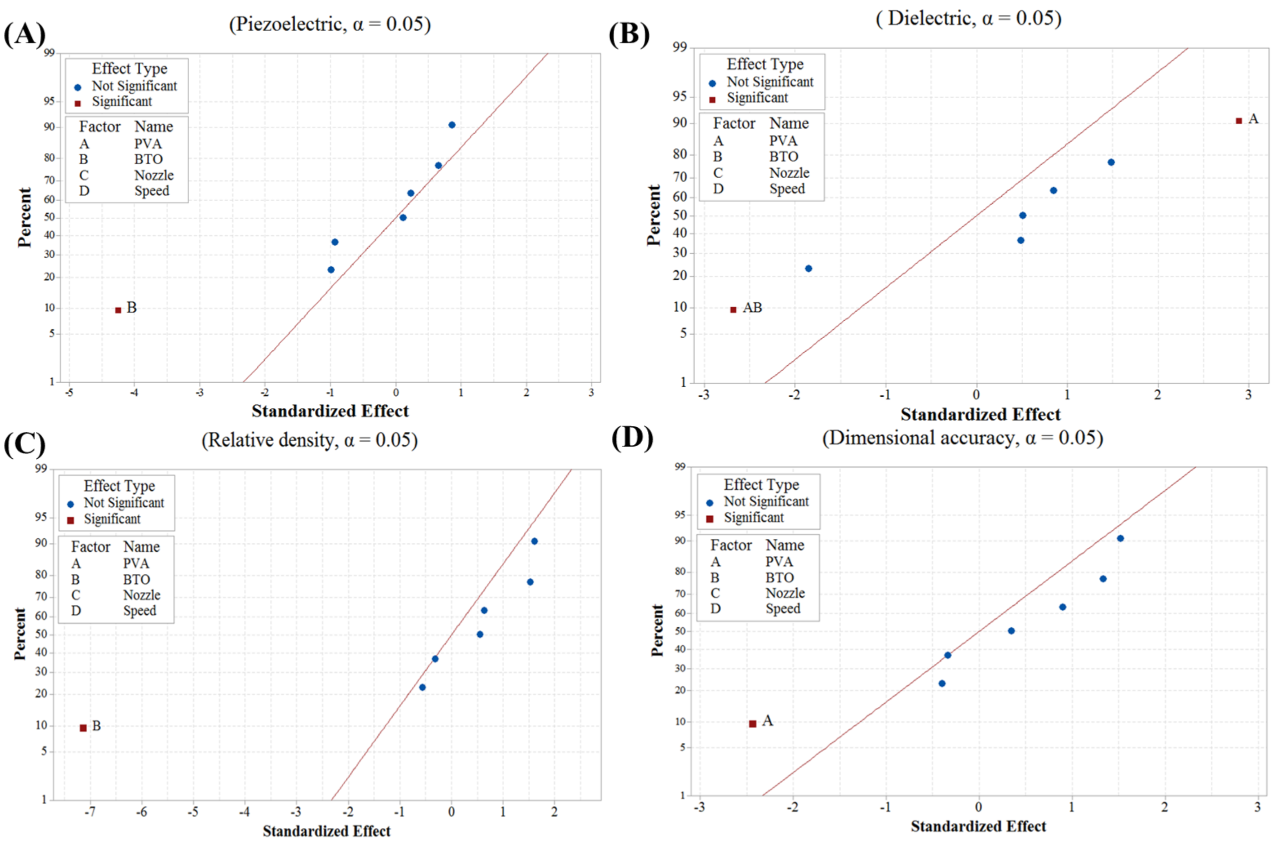

Figure 3.7: Normal probability plot of the standardized effects for A) piezoelectric coefficient B) dielectric permittivity C) relative density D) dimensional accuracy

Based on the results obtained in the factorial 2k-1 design, it was found that the parameters that positively affect the end-outputs are 100 nm BaTiO3 and 13 wt. % PVA concentration. There is no evidence to claim that the printing speed and the nozzle diameter affects the output evaluated in this study. Therefore, to optimize the fabrication of BaTiO3 ferroelectric ceramics, the printing speed and nozzle diameter can be neglect and used either level of said factors. The probability cube plot (Figure 3.14 to Figure 3.17) considered a fitted means analysis, which is useful to predict the outputs in a balanced design. The fitted means analysis indicates that 100 nm BaTiO3 and 13 wt. % PVA concentration enables the fabrication of ferroelectric ceramics with a piezoelectric coefficient higher than 200 pC/N. Dielectric permittivity is predicted to be higher than 2200. The density is predicted to be about 90 % with respect to the theoretical value of pure BaTiO3. Additionally, a low angle of deformation of about 10 degrees can be achieved. These predicted outputs are comparable with the BaTiO3 theoretical values, proving its capabilities to use FEF 3D printing technique for the fabrication of complex geometries for commercial applications.

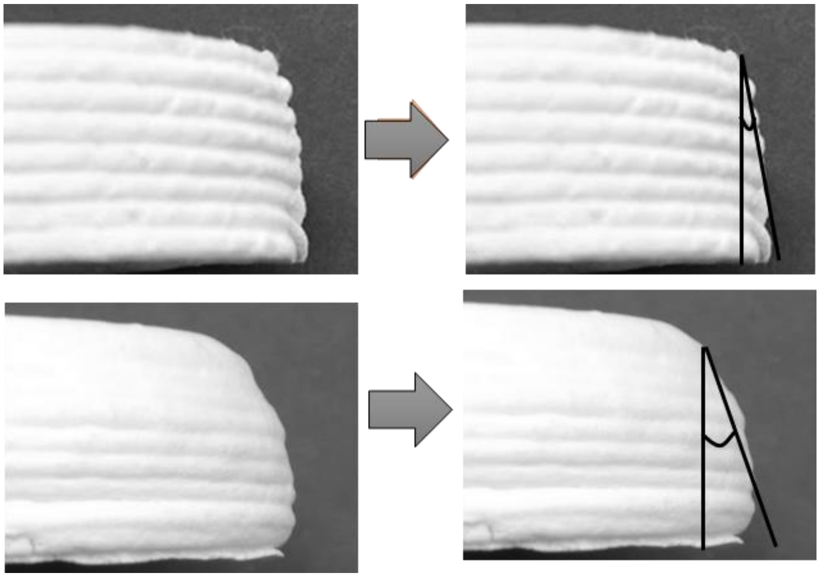

Figure 3.8: Paste deformation measurement after drying.

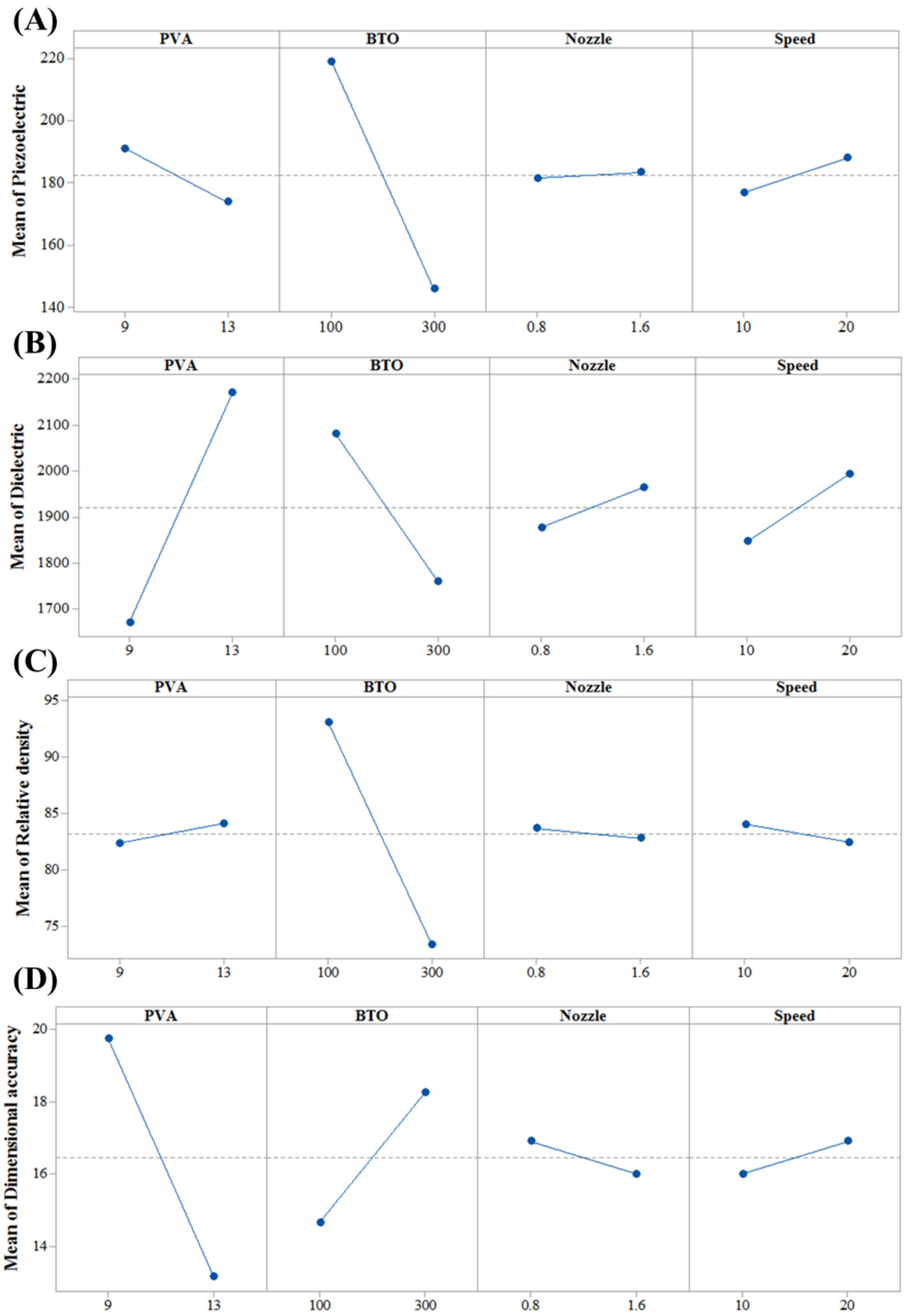

Figure 3.9: Main effect plot for A) piezoelectric coefficient B) dielectric permittivity C) relative density D) dimensional accuracy.

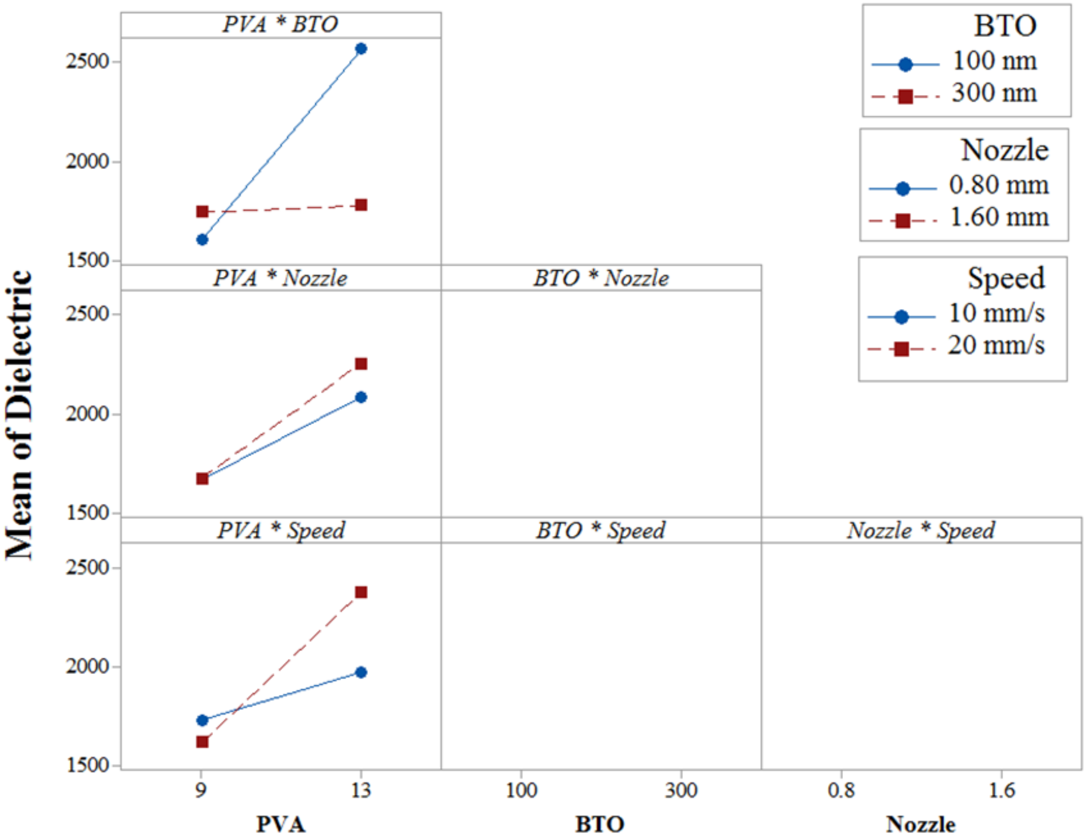

Figure 3.10: Interaction plot for dielectric permittivity

Table 3.3: Density results of green bodies.

Standard Order	**Run Order**	**PVA**	**BTO**	**Nozzle**	**Speed**	**Density (g/cm^3)**	**Relative density**
12	1	+	+	-	-	2.169	36.04%
3	2	-	+	-	+	2.062	34.24%
17	3	-	-	-	-	1.304	21.66%
11	4	-	+	-	+	2.092	34.75%
19	5	-	+	-	+	2.007	33.34%
23	6	-	+	+	-	1.574	26.15%
22	7	+	-	+	-	1.885	31.31%
14	8	+	-	+	-	1.800	29.89%
18	9	+	-	-	+	1.280	21.26%
8	10	+	+	+	+	2.087	34.66%
15	11	-	+	+	-	1.596	26.51%
20	12	+	+	-	-	1.949	32.37%
4	13	+	+	-	-	1.578	26.21%
5	14	-	-	+	+	1.567	26.03%
16	15	+	+	+	+	2.151	35.73%
9	16	-	-	-	-	1.884	31.29%
24	17	+	+	+	+	2.073	34.43%
21	18	-	-	+	+	1.614	26.81%
2	19	+	-	-	+	2.467	40.99%
10	20	+	-	-	+	2.479	41.17%
6	21	+	-	+	-	2.560	42.52%
7	22	-	+	+	-	1.723	28.62%
1	23	-	-	-	-	1.333	22.15%
13	24	-	-	+	+	2.299	38.18%

Table 3.4: Density after sintering

Standard Order	Run Order	PVA	BTO	Nozzle	Speed	Density (g/cm^3)	Relative density
12	1	+	+	-	-	4.719	78.40%
3	2	-	+	-	+	4.030	66.95%
17	3	-	-	-	-	5.958	98.97%
11	4	-	+	-	+	4.229	70.25%
19	5	-	+	-	+	4.256	70.70%
23	6	-	+	+	-	4.177	69.40%
22	7	+	-	+	-	5.179	86.04%
14	8	+	-	+	-	5.402	89.75%
18	9	+	-	-	+	5.711	94.87%
8	10	+	+	+	+	4.578	76.05%
15	11	-	+	+	-	4.004	66.52%
20	12	+	+	-	-	4.529	75.25%
4	13	+	+	-	-	4.219	70.09%
5	14	-	-	+	+	6.014	99.91%
16	15	+	+	+	+	4.752	78.94%
9	16	-	-	-	-	6.173	102.55%
24	17	+	+	+	+	4.761	79.09%
21	18	-	-	+	+	4.418	73.40%
2	19	+	-	-	+	5.863	97.39%
10	20	+	-	-	+	5.222	86.75%
6	21	+	-	+	-	5.806	96.45%
7	22	-	+	+	-	4.852	80.60%
1	23	-	-	-	-	5.666	94.13%
13	24	-	-	+	+	5.844	97.09%

Table 3.5: Piezoelectric coefficient results

Standard Order	Run Order	PVA	BTO	Nozzle	Speed	Piezoelectric coefficient (pC/N)
12	1	+	+	-	-	110.0
3	2	-	+	-	+	150.0
17	3	-	-	-	-	193.9
11	4	-	+	-	+	140.0
19	5	-	+	-	+	135.0
23	6	-	+	+	-	124.0
22	7	+	-	+	-	190.5
14	8	+	-	+	-	170.0
18	9	+	-	-	+	201.5
8	10	+	+	+	+	132.9
15	11	-	+	+	-	134.8
20	12	+	+	-	-	194.0
4	13	+	+	-	-	128.0
5	14	-	-	+	+	206.3
16	15	+	+	+	+	208.0
9	16	-	-	-	-	266.0
24	17	+	+	+	+	94.0
21	18	-	-	+	+	243.1
2	19	+	-	-	+	283.8
10	20	+	-	-	+	167.5
6	21	+	-	+	-	204.2
7	22	-	+	+	-	197.9
1	23	-	-	-	-	206.9
13	24	-	-	+	+	292.8

Table 3.6: Dielectric relative permittivity results

Standard Order	Run Order	PVA	BTO	Nozzle	Speed	Dielectric permittivity
12	1	+	+	-	-	1324.13
3	2	-	+	-	+	1784.30
17	3	-	-	-	-	1724.55
11	4	-	+	-	+	1640.00
19	5	-	+	-	+	1629.29
23	6	-	+	+	-	1541.49
22	7	+	-	+	-	3158.10
14	8	+	-	+	-	2165.21
18	9	+	-	-	+	1740.74
8	10	+	+	+	+	1990.52
15	11	-	+	+	-	2125.78
20	12	+	+	-	-	1754.96
4	13	+	+	-	-	1388.78
5	14	-	-	+	+	1506.72
16	15	+	+	+	+	1903.29
9	16	-	-	-	-	1583.62
24	17	+	+	+	+	2296.80
21	18	-	-	+	+	1416.44
2	19	+	-	-	+	3354.24
10	20	+	-	-	+	2942.77
6	21	+	-	+	-	1720.10
7	22	-	+	+	-	1728.14
1	23	-	-	-	-	1645.97
13	24	-	-	+	+	1715.08

Table 3.7: Dimensional accuracy results

Standard Order	**Run Order**	**PVA**	**BTO**	**Nozzle**	**Speed**	**Dimensional accuracy (angle)**
12	1	+	+	-	-	18
3	2	-	+	-	+	22
17	3	-	-	-	-	10
11	4	-	+	-	+	17
19	5	-	+	-	+	17
23	6	-	+	+	-	10
22	7	+	-	+	-	4
14	8	+	-	+	-	7
18	9	+	-	-	+	20
8	10	+	+	+	+	20
15	11	-	+	+	-	30
20	12	+	+	-	-	15
4	13	+	+	-	-	16
5	14	-	-	+	+	25
16	15	+	+	+	+	23
9	16	-	-	-	-	30
24	17	+	+	+	+	10
21	18	-	-	+	+	20
2	19	+	-	-	+	8
10	20	+	-	-	+	8
6	21	+	-	+	-	9
7	22	-	+	+	-	21
1	23	-	-	-	-	22
13	24	-	-	+	+	13

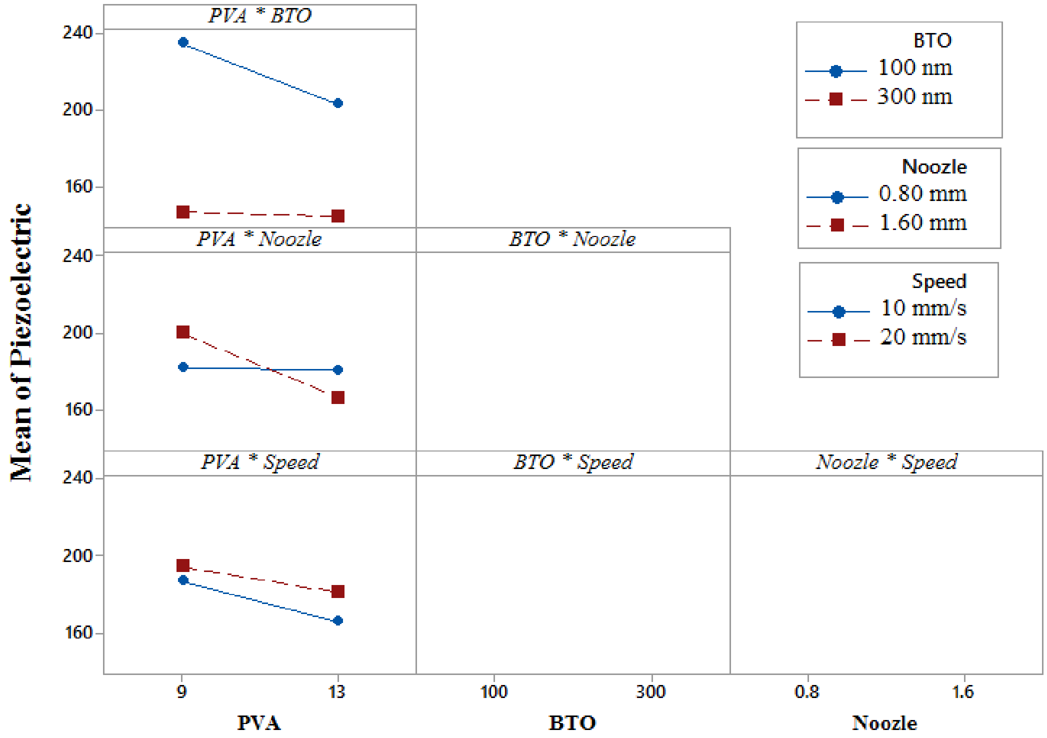

Figure 3.11: Interaction plot for the piezoelectric coefficient.

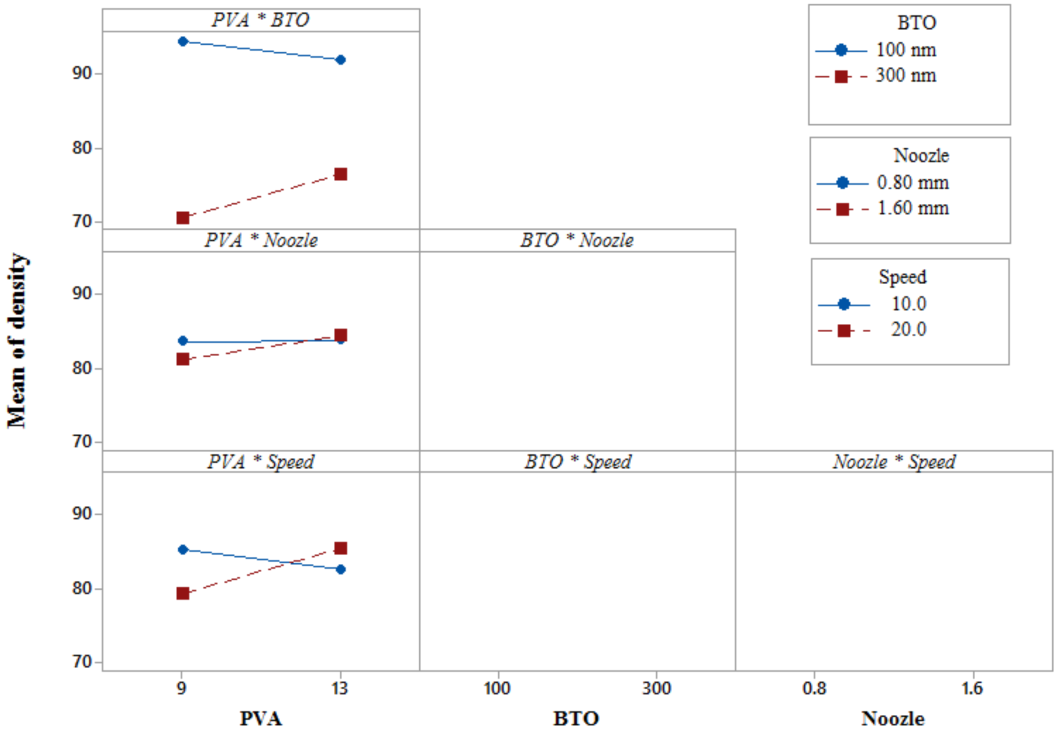

Figure 3.12: Interaction plot for relative density.

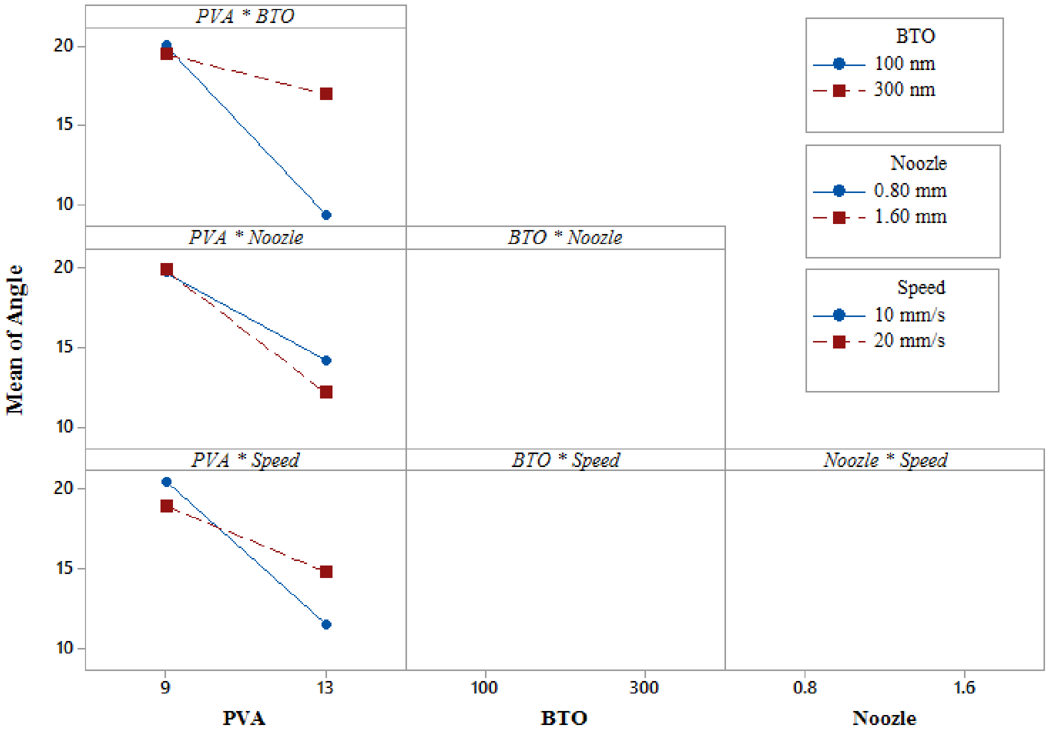

Figure 3.13: Interaction plot for dimensional accuracy.

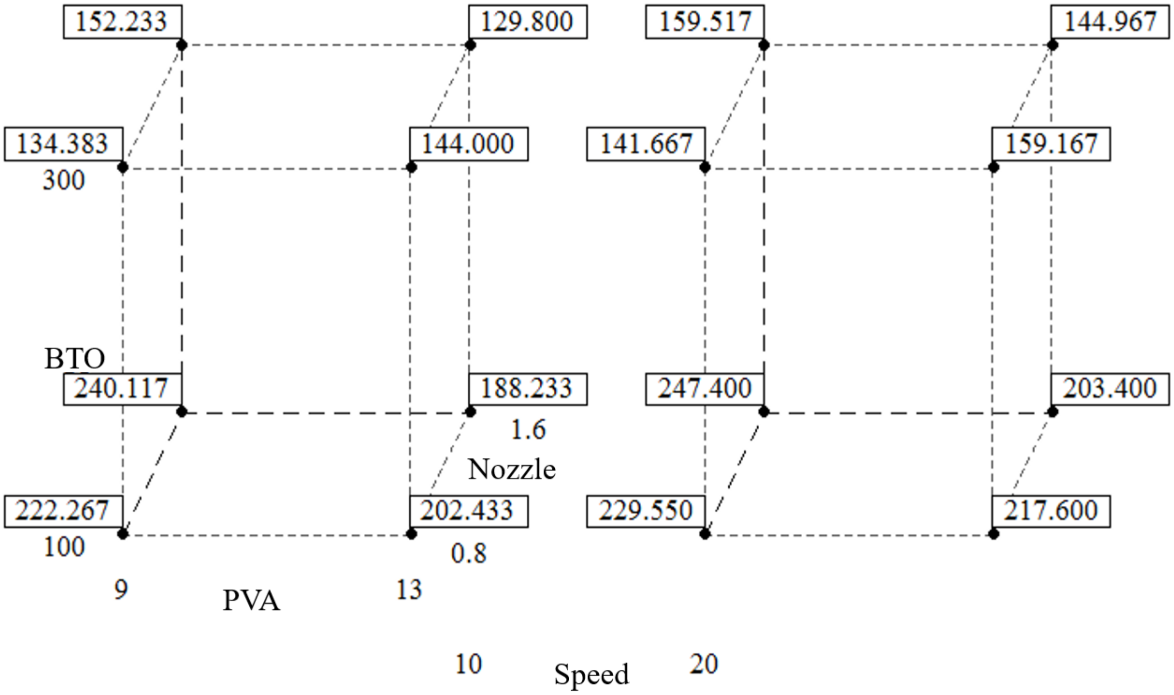

Figure 3.14: Probability cube plot for the piezoelectric coefficient.

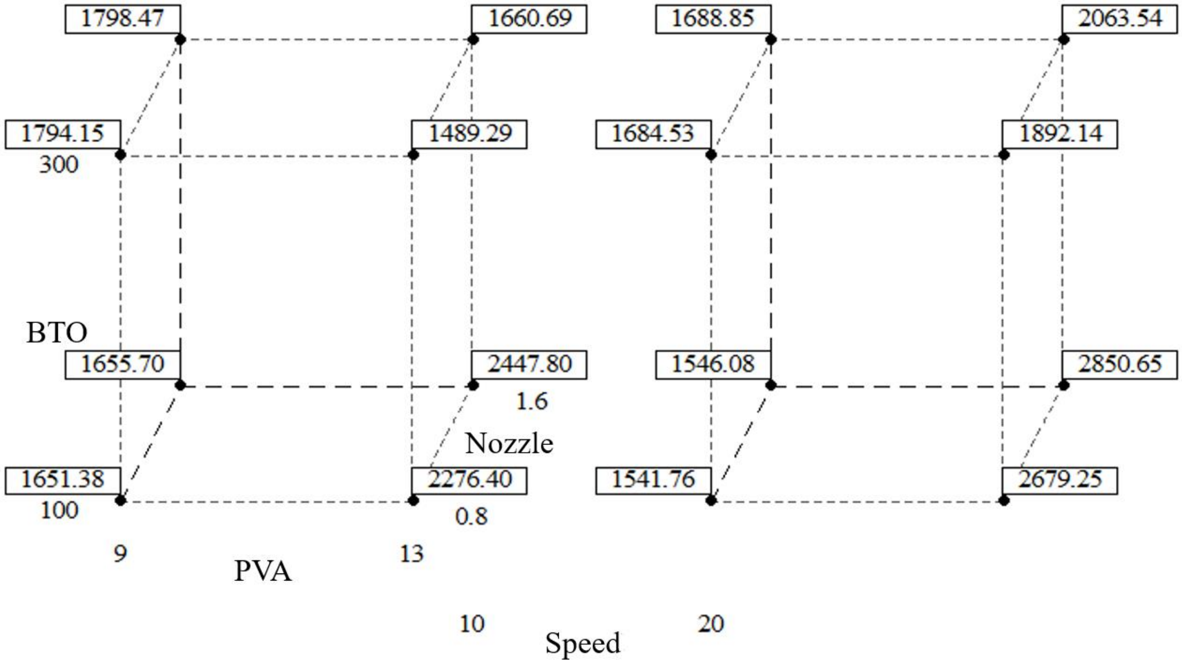

Figure 3.15: Probability cube plot for the piezoelectric coefficient.

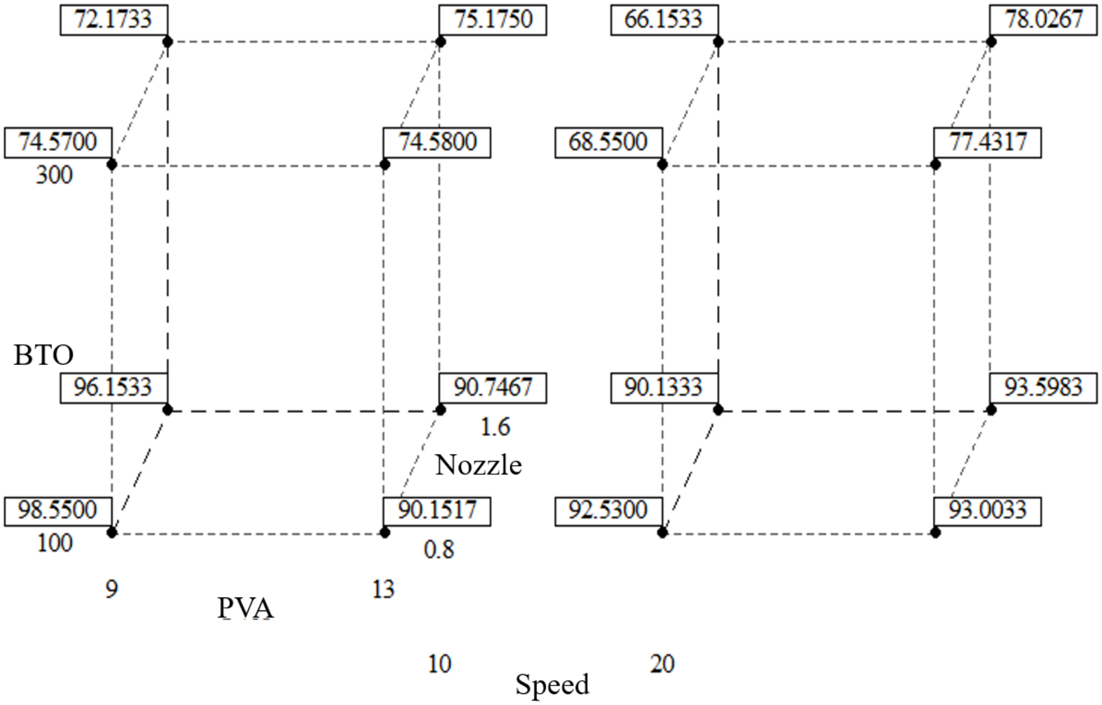

Figure 3.16: Probability cube plot for relative density.

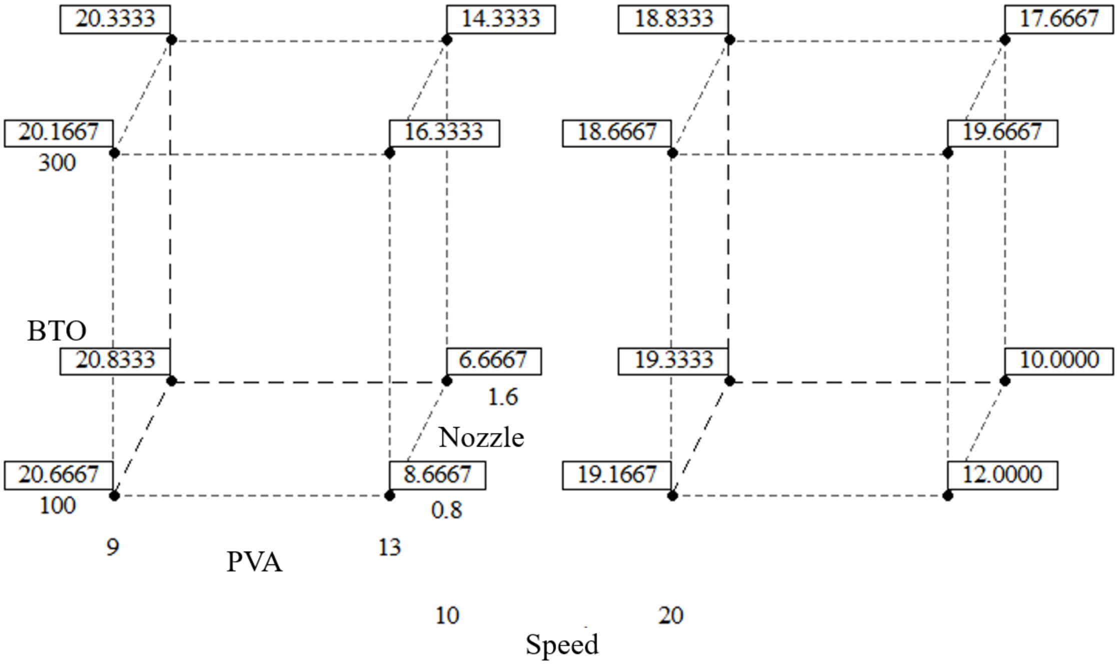

Figure 3.17: Probability cube plot for dimensional accuracy.

3.3 Conclusion

A DOE for BaTiO3 ferroelectric ceramics using FEF 3D printing technique was presented. This paper aimed to optimize the formulation of the ceramics suspensions to produced defects-free samples. This study considered the evaluation of BaTiO3 particle size, PVA concentration, printing speed, and nozzle diameter. Results showed that the BaTiO3 particle size positively affects the piezoelectric coefficient, dielectric permittivity and density of the samples. In another hand, it was found that the PVA concentration has an impact on dielectric permittivity and dimensional accuracy. The optimal levels are 100 nm for BaTiO3 and 13 wt. % PVA concentration. The printing speed and nozzle diameter do not influence the desired end-product outputs. Using the optimal levels in the paste formulation, it is possible to fabricate samples with 90 % density. A piezoelectric coefficient higher than 200 pC/N and a dielectric permittivity higher than 2200 can be obtained. Additionally, a low angle of deformation of about 10 degrees can be achieved, which is a good parameter for dimensional accuracy. These results correspond to the full theoretical properties normally achieve by traditional manufacturing techniques for BaTiO3 ceramics. Therefore, this paste extrusion technique can be used in the fabrication of more complex geometries and extend the applications of piezoelectric ceramics for sensors and actuators with designed geometry.

Chapter 4: Influence of bimodal particle distribution on material properties of BaTiO3 fabricated by paste extrusion 3D printing

Barium titanate (BaTiO3) is a lead-free piezoelectric ceramic widely used in sensors and actuators applications. However, there are many manufacturing challenges to process BaTiO3 due to the brittle nature of ceramics. Most current sensors based on piezoelectricity are limited to mold shapes or flat 2D structures, which narrow their applications. Paste extrusion (PE) 3D printing technique allows the fabrication of complex geometry ceramics with less design limitations. However, the piezoelectric property of 3D printed ceramics is typically lower than those fabricated using traditional means due to lower density. Herein, a study to evaluate the influence of bimodal particle distribution on improving density and piezoelectricity of BaTiO3 ceramics fabricated using PE 3D printing is presented. 3D printed and compression pressed samples under the same mixing ratios were compared. The highest packing density was obtained using 50-50% vol. fraction of bimodal particles for both types of samples. A predictive model for packing density was validated by experimental results. The highest piezoelectric coefficient of 350 pC/N was obtained using 50-50% vol. bimodal particle distribution. This piezoelectric coefficient is 40 % higher than the monodispersed sample using 100 nm particles with a piezoelectric coefficient of 250 pC/N.

4.1 Introduction

Barium titanate (BaTiO3) is one of the most reported lead-free piezoelectric ceramics due to the wide variety of industrial and commercial applications that it can be used [59]. Furthermore, BaTiO3 offers material properties that makes it suitable for sensors, capacitors and energy harvesting devices [2,3,6,59,60]. BaTiO3 is distinguished to have a good piezoelectric coefficient (d33: ~190 pC/N) [6] and high-dielectric permittivity (ε ~1700 at room temperature) [59]. Another well-known piezoelectric ceramic is lead oxide titanate (Pb[ZrxTi1-x]O3 or PZT), which returns in high piezoelectric properties (d33: ~500-600 pC/N), making it suitable for many industrial applications [6]. However, there is a lot of concern regarding the damage that it could produce to the environment and the human being. Since PZT contains high levels of lead oxide (PbO), many researches opted to use and optimize lead-free materials, such as BaTiO3. Nowadays, there are several traditional methods that can be used to fabricate bulk ceramics, including BaTiO3 such as slip casting, tape casting, extrusion, and injection molding [61,62]. Nonetheless, ceramics are brittle by nature and most of the designs have been restricted to 2D structures such as thin/thick films. Many efforts have been focused on the fabrication of ceramics without compromising theoretical materials properties. Several studies reported that the piezoelectric properties of BaTiO3 have a strong dependency on the powder particle size, which affects the grain growth of the ceramics [33,44]. Large powder particles require a higher change in energy, which leads to a lower grain growth during sintering, producing more voids in the samples which narrows the material's properties [8]. In contrast, the incorporation of small particles with large particles is found to improve green packing density [30,58]. The surface finish of the samples can also be improved with the use of bimodal particle distribution, since the small particles help to fill the voids in between the larger particles [63,64]. Although the use of bimodal powder mixtures could lead to higher packing densities, it might not necessarily result in a higher densification rate. However, the use of bimodal particles helps to control the shrinkage rate and improve mechanical strength [38,65,66]. Moreover, determining the powder mixture ratio that will optimize the results is still a challenge. Many efforts have been done in an attempt to develop mathematical models to predict packing density and sintering behavior of spherical powders with bimodal distribution [36,64,67]. Nonetheless, there is little experimental work in the area of piezoelectric ceramics that incorporate a mathematical predictive model to determine the optimal packing density and mixture of powders while minimizing the shrinkage of the samples after sintering.

Additive manufacturing (AM) frequently referred as 3D printing, is a manufacturing technology commonly used for rapid prototyping to fabricate three-dimensional parts from a CAD design. The American Society for Testing and Materials (ASTM) group F42 divides AM on seven categories: vat photopolymerization (VP), powder bed fusion (PBF), material jetting (MJ), binder jetting (BJT), material extrusion (ME), sheet lamination (SL) and direct energy deposition (DED). AM enables the possibility to expand ceramic fabrication through complicated design and low cost. Among the advantages of 3D printing are the possibility of using a wide variety of materials, high design complexity, and reduced fabrication time [41]. Different additive manufacturing techniques, such as selective laser sintering (SLS) [68], BJT [69,70], and ink-jet printing [63] have evaluated bimodal particle distribution to increase material properties. However, ceramics fabricated by SLS or BJT although resulted in better surface finish and improved density, the samples yet showed high levels in porosity affecting material properties. Additionally, very limited work has analyzed the use of bimodal particles to increase final density of functional ceramics with improved functional properties using additive manufacturing. Paste extrusion (PE) is a ME 3D printing technique that selectively deposits a viscous slurry through a nozzle to form a three-dimensional object, including ceramics in a relatively short period of time [71]. PE technique can be used to extrude different types of materials by incorporating a binder, plasticizer and/or a lubricant to control the rheological properties of the slurry. However, one of the main drawbacks is the resolution of the 3D printed parts due to the nature of the slurry. For that reason, the rheological properties play a critical role to obtain good viscoelastic properties that guarantee self-support during printing. Despite that, PE slurries are easy to modify for specific applications, such as bimodal mixtures without affecting its printability due to the incorporation of rheological modifiers. Additionally, PE technique offers a variety of methods to trigger a liquid to solid transition in the paste that allows to retain structural shape during printing. A partial liquid phase evaporation of the paste could be achieved at room temperature after deposition on the substrate due to solvent evaporation [15]. In addition, liquid phase curing could be achieved through the incorporation of photocurable monomers dispersed in the paste. For this technique, UV-light is used to start the photopolymerization reaction in the paste, which has been reported as a fast process to solidify samples [72]. Another method for a controlled liquid to solid transition is by using a fluid medium (i.e., mineral oil) under heating [18]. Lastly, liquid to solid transition is possible by liquid phase freezing of the paste that allow to solidify the samples after deposition on the substrate by freezing [72]. In addition, as-printed parts should be subjected to a post-treatment process to dry them without inducing any quality issue, such as warps or cracks, which could be considered as another drawback of PE. Nonetheless, several studies demonstrated that PE technique enables the fabrication of high-density ceramics, achieving above 90% of theoretical density when using nanoparticles [16–18,21,35,58]. To the best of our knowledge, the use of bimodal mixtures to enhance piezoelectric properties of ceramics by PE technique has not been reported before and for this reason its impact should be evaluated.

Two different particle sizes were studied to predict the maximum green packing density using bimodal mixtures and compared with experimental results. BaTiO3 ceramics were fabricated using PE technique and compared with hydraulic pressed disks to evaluate the capabilities of using 3D printing technique for piezoceramics. Furthermore, the effect of shrinkage for bimodal mixtures after sintering was analyzed as well as its impact on final density, and piezoelectric coefficient. This experimental methodology aims to demonstrate superior material properties by the incorporation of bimodal powder particle distributions to fabricate high-density ceramics by additive manufacturing.

4.2 Experimental details

4.2.1 Materials, Synthesis and Fabrication

Two different particle sizes of BaTiO3 powder (100 nm and 400 nm; Ba to Ti ratio 0.999-1.001; Inframat, Manchester, CT) were used to evaluate the influence of bimodal particle distribution on density and piezoelectric coefficient for PE technique. Polyvinyl alcohol (PVA) powder (Mw ~ 89,000-98,000; Sigma Aldrich, St. Louis, MO) was used as a binder and polyacrylic acid (PAA) was used as a lubricant (Sigma Aldrich, St. Louis, MO) for the slurry fabrication. The slurry was prepared as detailed described in previous works [35], varying the BaTiO3 content with different amounts of large and small particles. PAA was added as a rheological modifier for the slurries and to facilitate the printing process.

The samples were printed using a Printrbot Simple Metal 3D printing machine with a modified slurry dispersion head. The 3D printer structure consists of a force-controlled piston that applies force over the syringe to selectively extrude the ceramic paste through a nozzle and deposits it onto an aluminum plate. Samples with dimensions of 25 x 10 x 8 mm were printed using a 600 µm inner diameter nozzle. Figure 4.1 illustrates PE printing process of BaTiO3 and the 'as-printed' sample. After deposition, the samples required a controlled solvent evaporation process to prevent cracks from being generated. The printed samples were immediately placed in a freezer at -5 °C for 2 hours to promote some initial water evaporation by sublimation. Samples were then placed in an oven at 40 °C for 24 hours to remove most of the water content and retain structural shape. Additionally, BaTiO3 disks of 1-inch (25.4 mm) diameter were fabricated through hydraulic press using the same ratios as the 3D printed samples. Different amounts of large and small particles of BaTiO3 were mixed using a vortex mixer for 2 minutes. Finally, the samples were fabricated using 6 g of ceramic powder and applying 29.4 kN force (58.02 MPa) for 5 minutes.

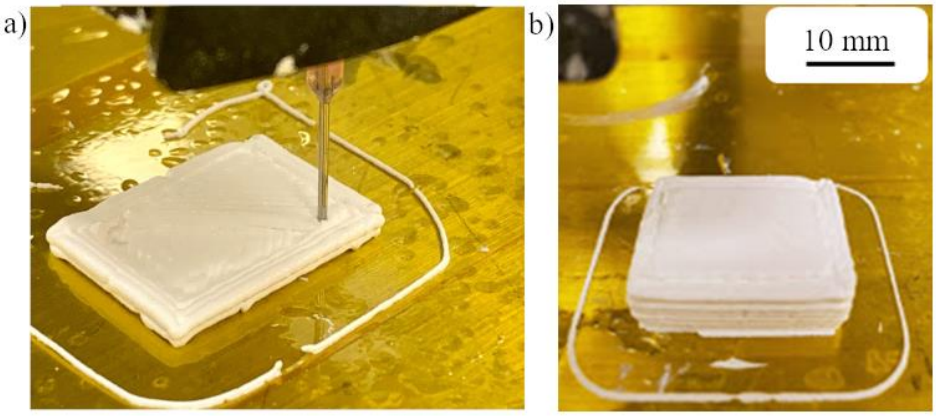

Figure 4.1: a) Printing process of BaTiO3 ceramics using PE technique. b) 'As-printed' sample before drying.

4.2.2 Post-Processing

The 3D printed and pressed samples were subjected to a sintering process to enhance grain growth thus densifying the ceramic. The samples were debinded at 600 °C for two hours using 4 °C/min ramp to completely burn out the polymer binder. Then, the samples were sintered at 1250 °C for two hours with a 4 °C/min ramp. Lastly, samples were cooled down at 4 °C/min to room temperature. After sintering, the samples were polished using 240-grit sandpaper. Conductive silver paint (SPI supplies, West Chester, PA) was then applied on top and bottom surfaces and dried at 150 °C for 20 minutes. Thermal poling was performed by applying a 5.4 kV/cm electrical field on the samples submerged in silicon oil at 80 °C for two hours [73–75]. Piezoelectric coefficient was measured 24 hours after the poling process.

3.2.3 Material Characterization

Rotational rheological measurements for the bimodal ceramic suspensions were performed in a DHR-2 rheometer (TA Instruments, New Castle, DE) with a parallel plate geometry. The test was performed at 25 °C with a 0.7 mm gap between the plates. The relative density of the samples was measured by Archimedes' method at 25 °C using deionized water as medium. The results in density were compared with the theoretical value of pure BaTiO3 of 6.02 g/cm3 [53]. Grain morphology of the BaTiO3 samples were characterized from the cross sectional surface fracture by using scanning electron microscopy (SEM; JEOL, JSM-IT500HR) under low vacuum, 20.0 kV accelerating voltage using backscatter electron. Diffraction patterns were obtained on a PANanalytical Empyrean system using Cu-Kα radiation (λ = 1.5418 Å) equipped with a PIXcel [3D] detector. The piezoelectric coefficient was calculated using a d33 meter (APC YE2730A) by applying a load of 0.25 N at a frequency of 110 Hz. The dielectric constant of the samples was determined by measuring the capacitance using an LCR meter (1920 Precision, IET Lab) at room temperature (25 °C) at a frequency of 1 kHz.

3.2.4 Predictive Model for Green Packing Density

The predictive model for green packing density [64] considers two spherical powders of the same material, a large powder L and a small powder S. Different mixture compositions X will lead to a different packing density f, where X* corresponds to the maximum peak for packing density f*

$$f^{*}=f_{L}+(1- f_{L})f_{S} \qquad (1)$$

$$X^{*}= f_{L} / f^{*} \qquad (2)$$

where f_L corresponds to the packing density of the large powder and f_S to the packing density of the small powder. However, another factor that has to be considered is the homogeneity H of the mixed powders, which will be influenced by the mixing technique and overall distribution of small and large powders.

$$V_{r}=V_{S}-X(V_{S} -V_{L}) \qquad (3)$$

$$V= V_{r} -dV^{*}_{D} XH/ X^{*} \quad \text{for } X<X^{*} \qquad (4)$$

$$V= V_{r} - dV^{*}_{D} H(1-X)/(1-X^{*}) \quad \text{for} > X^{*} \qquad (5)$$

here Vr is defined as the specific volume of the mixture, which is determined in terms of the volume of the small Vs and large VL particles and dV*D represents the specific volume change in terms of the two different particle size. The packing density will be inversely proportional to the volume (Eq. 4 and 5) for the different types of mixtures as a function of X*.

3.3 Results and Discussions

3.3.1 Rheological Measurements

The BaTiO3 ceramic suspensions were fabricated taking into consideration of the required rheological properties for PE technique. Different factors were considered to assure the printability of the suspension such as powder volume content, binder concentration and lubricant content. The printability of a ceramic suspension is highly influenced by the powder volume fraction content.

While suspensions with high powder volume fraction are desired due to possibility of return in density and material properties, suspensions with high powder volume fraction produce an increase on the viscosity, restricting particle mobility and affecting the printing process [25]. In addition, high viscous suspensions increase the probabilities of clogging due to particle agglomerates, producing a discontinuous flow deposition [56,76]. On the other hand, the use of bimodal particle distribution allows to reduce the viscosity using the same volume content by releasing the capillary forces in the suspension [77]. The powder volume content for the suspensions was determined based on the small particles since the viscosity will be higher than large particles suspensions [25,56,76]. The ceramic volume content was set to 28.5 vol. % for all the suspensions. This is in good agreement with literature as previous studies reported up to 30 vol. % for BaTiO3 slurry fabrication [2]. The binder concentration was selected based on the results obtained from previous works as it was found to contribute to a higher storage modulus (G'), improving shape retention [35]. Figure 3.2 (a) shows the viscosity of the suspensions as a function of the applied shear rate for different mixing ratios of small and large particles. The monodispersed suspension of 400 nm BaTiO3 showed a drastically decrease in viscosity compared to 100 nm BaTiO3. The increase in viscosity for small powder particle suspensions could be attributed to a higher contact between the particles which trapped liquid inside aggregates of powder [28]. All of the ceramic suspensions showed a shear thinning behavior, which can be attribute to the binder that acts as a non-Newtonian fluid that modifies the viscoelastic properties at different applied shear rates [55]. In a similar way, the yield stress for the monodispersed suspensions showed a drastically decrease for large particles as shown in Figure 4.2 (b). The increase in the yield stress for narrow particles can be attributed to a stronger interparticle network producing higher binding forces caused by stronger hydrogen bonding similar to a solid like properties [78]. It was observed from Figure 4.3 that the incorporation of large particles to replace some of the small particles helped to reduce the relative viscosity of the suspension. This is in good agreement with literature as a decrease in the viscoelastic properties is expected when the modality of a suspension changes from unimodal to bimodal using a fixed volume content [77]. The decrease in yield viscosity could be attributed to space release in between the particles matrix, increasing the mobility of the particles [76,77].

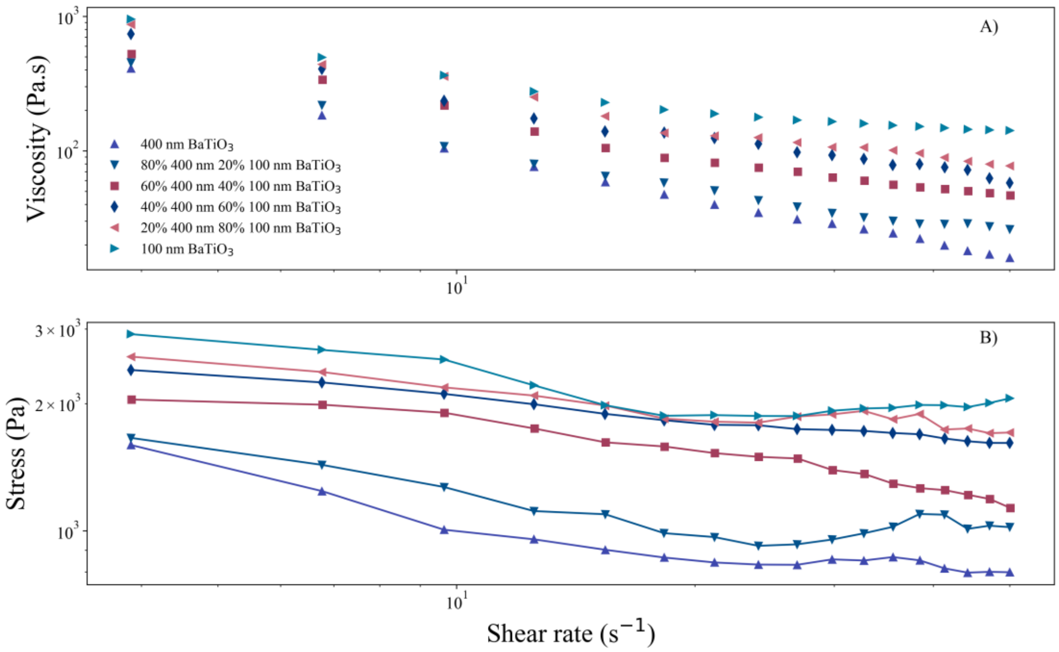

Figure 4.2: (A) Evolution of viscosity as a function of shear rate for monodispersed slurries and bimodal particle distribution with different mixing ratios of BaTiO3. (B) Required applied stress as a function of shear rate for different BaTiO3 slurries, monodispersed and bimodal particle distribution.

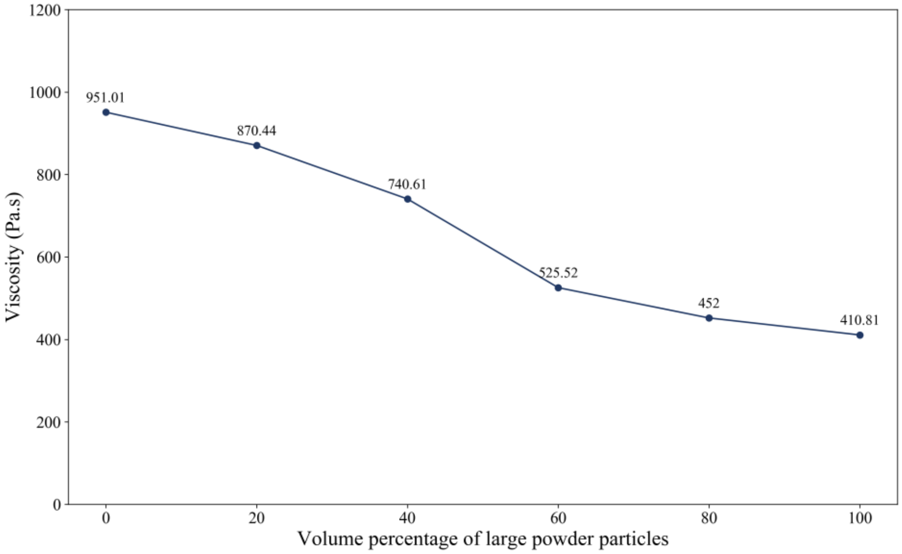

Figure 4.3: Initial viscosity of the slurries at different bimodal particle distribution ratios.

3.3.1 Density Analysis

The packing density for both the 3D printed and pressed samples before sintering is shown in Figure 4.4. An increase in packing density through the incorporation of small particles was observed until the maximum peak between 40-60 % vol. percentage (60 % vol. percentage for 3D printed samples and 40 % vol. percentage for pressed bodies) was reached. Then, the packing density started to decrease again, with a packing density in the range of 30 % (~1.806 g/cm3) for 3D printed samples and 51 % (~3.01 g/cm3) for the pressed disks. The results obtained for the packing density are in good agreement with literature, as previous studies obtained similar trends for different volume fractions of alumina powders [79,80]. The predictive model for bimodal powder mixtures to calculate the maximum peak for packing density is shown in Figure 5, which evaluates different homogeneity (H) values and compares them with experimental results. The highest packing density for the 3D printed samples can be obtained at 55.80 % vol. percentage of large powder particles as shown in Figure 4.5 (a). While the maximum peak of packing density for the pressed bodies was observed to be at 67.54 % vol. percentage of large powder particles as shown in Figure 4.5 (b). It was observed that the predictive model for the 3D printed samples fitted with 0.3 homogeneity while the pressed disks fitted with 0.1 homogeneity. From literature it is known that an H value of 1 represents the ideal arrangement of small and large particles but that scenario is not likely to happen, narrowing packing density. The difference in homogeneity from both types of samples was affected by the distribution of powders and mixing techniques as aforementioned. These differences in homogeneity lead to different packing densities and therefore, the homogeneity of the model is determined by experimentation [64,79]. The experimental data showed a maximum packing density at 50 vol. % for the 3D printed samples with 35.99 % (~2.16 g/cm3) and the pressed samples with 53.62 % (~3.23 g/cm3) relative packing density with respect the theoretical value of BaTiO3. The change in the maximum packing density from the 3D printed compared with the pressed samples was expected to be lower due to the incorporation of the binder and the solvent in the slurry affecting the density and homogeneity of the powder dispersion. Furthermore, the binder matrix might produce agglomerations, decreasing in the optimal packing density for the 3D printed samples.

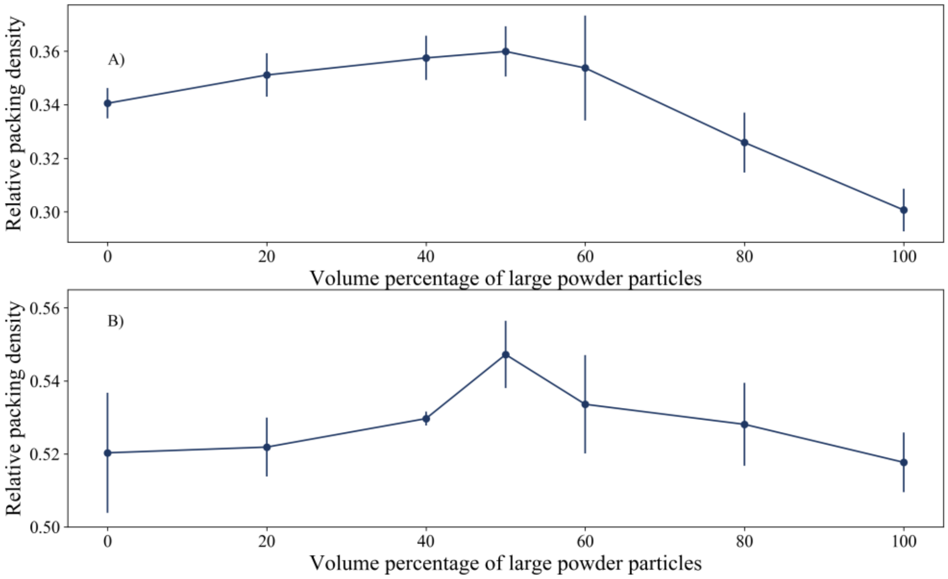

Figure 4.4: Packing density of the green bodies at different mixing ratios a) 3D printed samples b) Pressed samples.

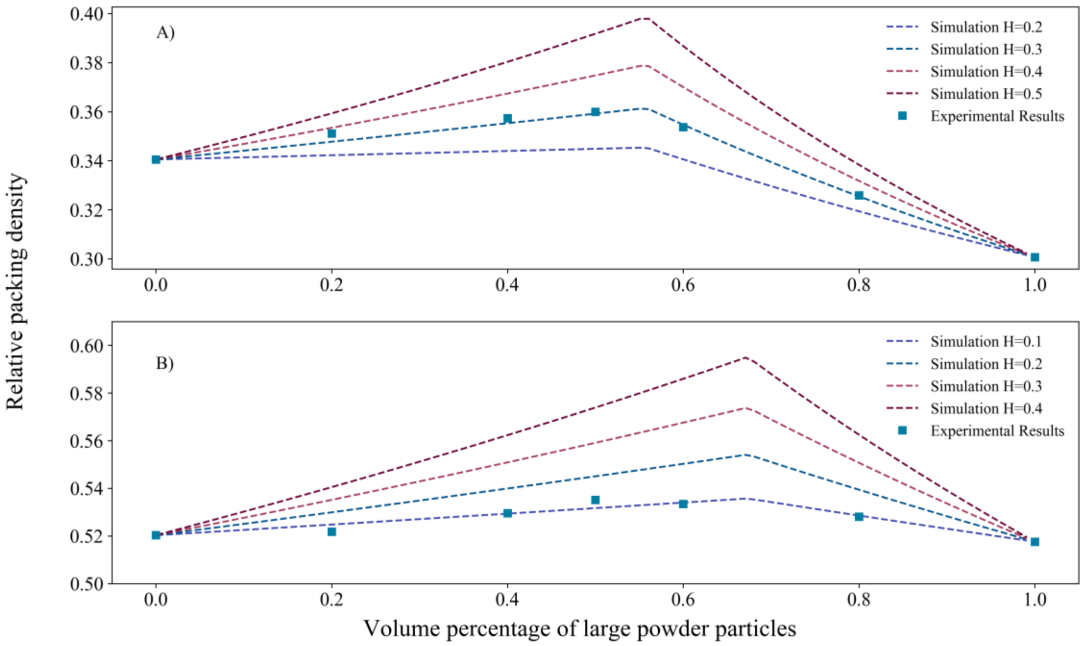

Figure 4.5: Predictive model for relative packing density a) 3D printed samples b) Pressed samples

The density after sintering for both the 3D and pressed samples are shown in Figure 6. The monodispersed samples with the small particle resulted in the highest final density (89.97 % for 3D printed and 92.16 % for the pressed samples), while the monodispersed samples with large particle returned in the lowest density (70.25 % for 3D printed and 81.21 % for the pressed samples). These results were expected as previous studies suggested that the energy required to enhance densification depends on the powder particle size [68]. From the results in density, it can be observed that the densification rate was affected by the volume content of small particles in the sample. A similar trending behavior was observed for both types of fabricated samples. In which, instead of following a linear decrease in density with the increase of large particles, it seems to present an inflection point at 50-50 vol. % indicating that the final density might be affected by the dominant powder size in the sample. This type of trend on density were observed for bimodal powder mixtures of Alumina [68]. In addition, large powder particles created a rigid skeletal structure that restricts the densification process, reducing shrinkage and increasing porosity in the samples [64,68,81]. These results are in good agreement with the shrinkage of samples as shown in Figure 4.7, which represent the change in volume after sintering. Furthermore, the incorporation of bimodal particles promotes surface diffusion during the initial and intermediate stages of sintering which contributes to grain growth and shrinkage compared with using large particles only [82].

Shrinkage is another indicator of densification; a higher shrinkage might be desired to obtain high-density ceramics. However, dimensional accuracy plays an important role in additive manufacturing and should be considered for user-end applications. The 3D printed samples showed a higher level of shrinkage than pressed disks of 3.947 % in average, which is due to the solvent evaporation and binder burnout during the sintering process. In a similar way as the results in density, the shrinkage percentage decreased when the volume fraction of large powder particles was increased. Furthermore, it seems to present an inflection point at 50-50 vol. % for both types of samples, presenting a linear decrease behavior in shrinkage. It was observed that the shrinkage of the 3D printed samples can be minimized to < 42 % by using large powder dominant mixtures and still get ceramics with > 71 % density with respect the theoretical value.

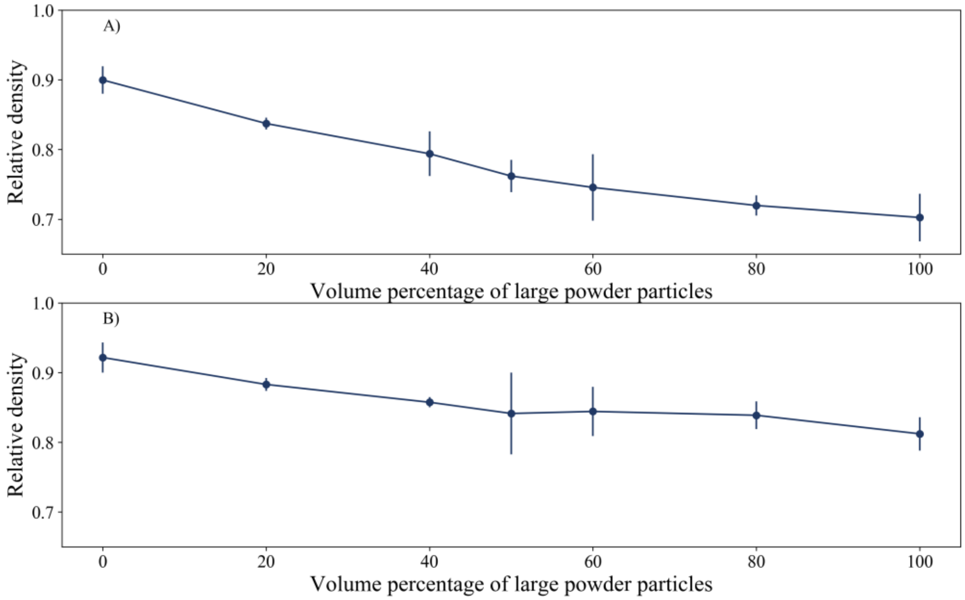

Figure 4.6: Relative density at different mixing ratios a) 3D printed samples b) Pressed samples.

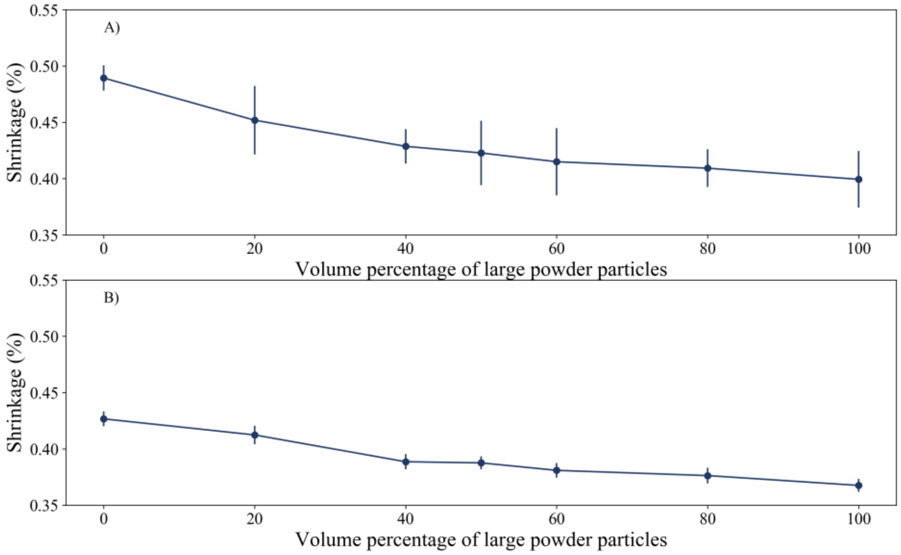

Figure 4.7: Shrinkage of the samples after sintering for a) 3D printed samples b) Pressed samples.

3.3.2 Morphology and piezoelectric property

The SEM analysis of the cross-sectional microstructure for different mixing ratios of the 3D printed samples after sintering is shown in Figure 4.8. The monodispersed samples from Fig. 4.8 a) and f) indexed for normal distribution of the final grain-growth with different levels of porosity. The small powder particle showed a higher grain-growth of 2.14 µm compared with the large powder with grain size of 1.45 µm after sintering as shown in Figure 4.9. The difference in grain-growth could be attributed to a lower change in energy required to enhance densification. Figure 4.8 b) and c) show the samples where the small powder particles were dominant in the mixture and the microstructure presents more agglomerations of large particles, similar to the monodispersed samples of 100 nm. This bimodal distribution on the grain-growth affected the average length reducing it to 2.01 µm in average while increasing the standard variation for small particle dominant mixtures. While Fig. 4.8 e) shows a sample with large powder particles dominant in the mixture and the microstructure more similar to the 400 nm with a grain growth of 1.44 µm. Lastly, the 50-50 vol. % sample showed agglomeration of big and small grains. However, the grain dispersion seems to be more homogeneously distributed as it was the mixture with the lowest grain variation 1.46 ± 0.277 µm. These different grain-growth behaviors are similar to results reported for technical ceramics [65,66,68] in which the levels of porosity are restricted by the dominant powder on the mixture.

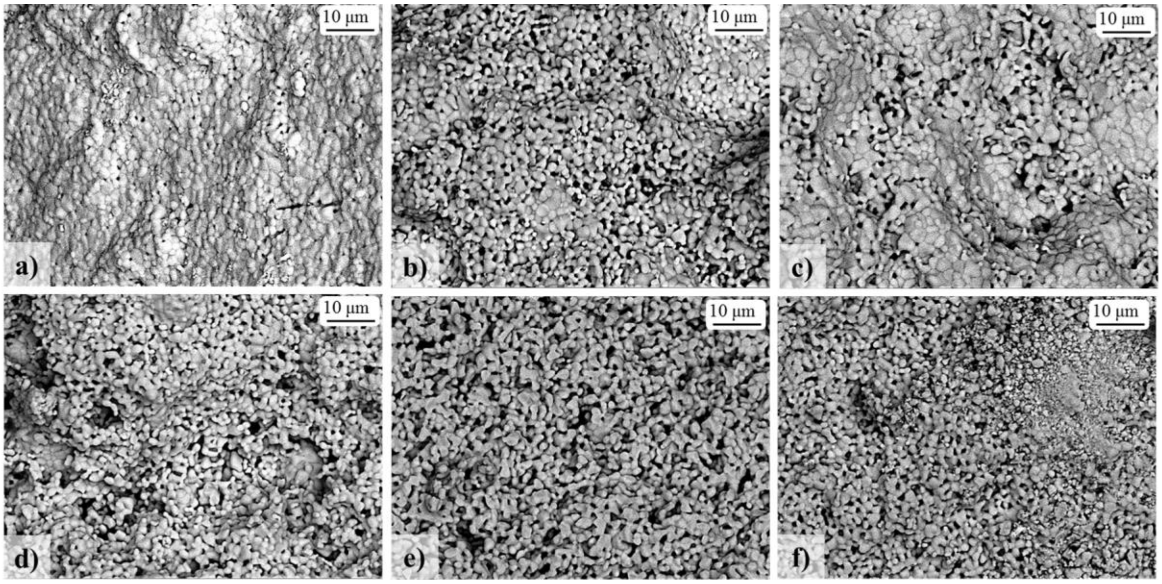

Figure 4.8: Evolution of grain-growth of 3D printed samples from the cross-sectional microstructure with the following mixture ratios a) monodispersed 100 nm b) 80 % 100 nm – 20 % 400 nm c) 60 % 100 nm – 40 % 400 nm d) 50 % 100 nm – 50 % 400 nm e) 20 % 100 nm – 80 % 400 nm f) monodispersed 400 nm.

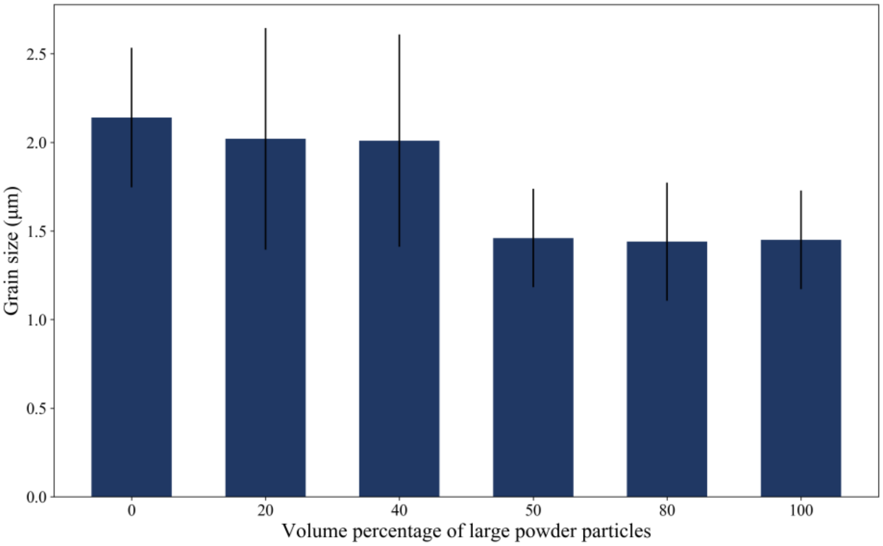

Figure 4.9: Grain length size of BaTiO3 of monodispersed and bimodal distribution samples.

The powder X-ray diffraction patterns (pXRD) for 100nm and 400 nm of BaTiO3 and bimodal mixture (50%-50% 100nm-400nm) are shown in Figure 10. After the sintering and poling processes, the pXRD patterns for the three samples were obtained in a range from 20 to 80 2θ degrees at room temperature. The diffraction patterns of BaTiO3 were indexed according to ICSD card no. 98-006-7520 and correspond to a tetragonal crystal system. All three diffraction patterns show the predominant peak at 31.53 2θ corresponding to the (011) planes and mayor peaks at 38.9, 44.8, 45.3, 51, 56.2 and 65.7 2θ degrees corresponding to planes (110), (002), (200), (120), (121) and (022), respectively. Peak splitting is observed in the range of 44 to 46 2θ degrees as shown in Figure 10 b) which represents a cubic to tetragonal phase transformation [4,31]. This lower symmetry phase change in the crystal structure of BaTiO3 leads to the ferroelectric properties of the ceramic. The peak splitting is expected when ceramics are subjected to heat treatments higher than 1000 °C [4]. Tetragonal crystal structure of BaTiO3 remains at room temperature and up to its Curie temperature of 120 °C where it loses its dipoles alignment and therefore losing its piezoelectric properties. The differences on degrees of crystallinity can be attributed to the final grain growth after sintering, since smaller powders require less energy during sintering. Therefore, it is expected to observe a higher tetragonality when using the 100 nm.

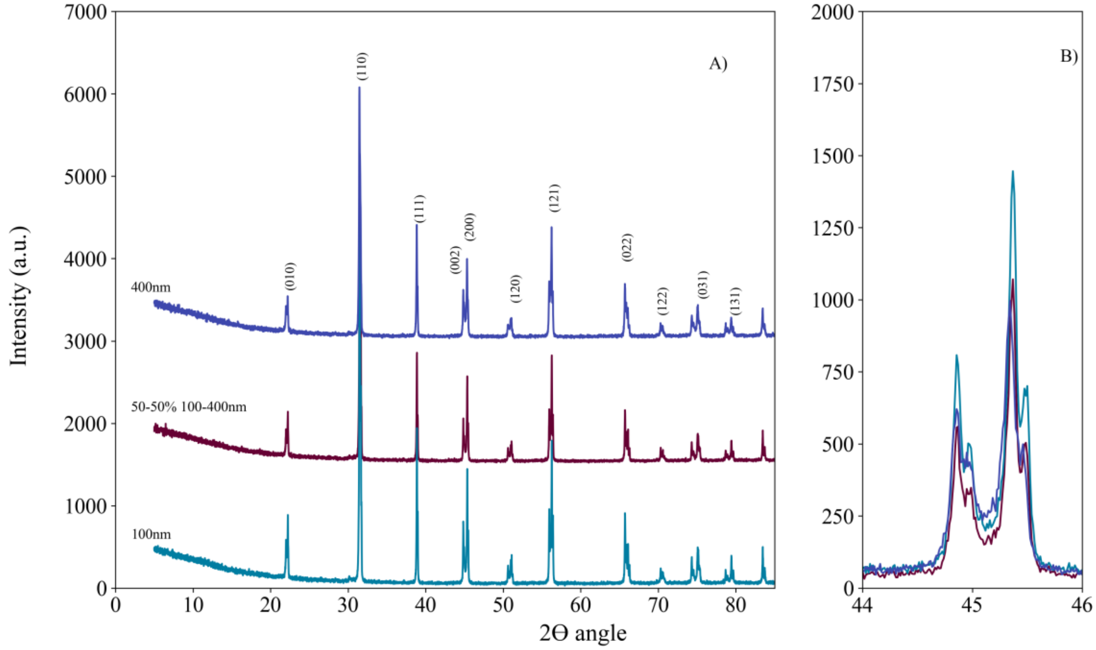

Figure 4.10: a) Powder X-ray diffraction patterns of BaTiO3 for 100 nm, 400 nm and 50-50% powder mixture b) XRD at peaks (002) and (200) in the rage 2θ from 44 to 46°.

Considering the functional properties of BaTiO3, the piezoelectric coefficient (effective d33) was evaluated. Figure 4.11 shows the piezoelectric coefficient of the 3D printed and pressed samples. The monodispersed samples with small powder particle had a superior piezoelectric property compared with the monodispersed samples with large powder particles. The same behavior was observed for 3D printed and pressed samples. A piezoelectric coefficient of 244.5 pC/N for 3D printed and 316.5 pC/N for pressed samples could be achieved using 100 nm. While for the 400 nm a piezoelectric coefficient of 175 pC/N for 3D printed and 180.2 pC/N for pressed. PE samples demonstrate the feasibility of using additive manufacturing to obtain similar material properties to the pressed samples with the possibility to expand to different application designs. For the bimodal mixtures, it was observed that the increment in volume percentage of large particles affected the piezoelectric property by decreasing its value. However, for the 50-50 vol. % samples, a highest peak in the piezoelectric properties was observed for both 3D printed and pressed disks of 350 pC/N. This represents an increment of 40% in the piezoelectric coefficient with respect to monodispersed sample of 100 nm with 15 % less density using PE technique.

The difference in the piezoelectric coefficients of BaTiO3 ceramics can be influenced by several factors, such as grain-growth, grain boundaries, domain walls, Ba to Ti atomic ratio, and porosity [83]. Studies on piezoelectric ceramics suggest that material properties could be influenced by the final density of the samples [53], and the grain-growth at the micron level for Ba to Ti atomic ratio ≥ 1 [44,83]. The tetragonal phase of BaTiO3 typically consist of two kinds of domain walls, antiparallel (180° walls) or perpendicular walls (90° walls) with respect the orientation of polarization. The domain arrangement and width depend on the grain size of the ceramic affecting the domain wall mobility, which contributes to the piezoelectric and dielectric properties [4]. Coarse ceramics with grain size above 10 μm have found to have antiparallel and perpendicular walls arrangements while ceramics with grain size below 10 μm show mostly perpendicular walls. Grain size at near 1 micron has been founded to be beneficial to the crystalline structure of BaTiO3 since a decrease in the 90° domain walls width is produced affecting the final piezoelectric response [8,84]. This decrease will facilitate the rotation of the domain walls increasing the sensibility to an external stimulus on stress or electrical signal [8,84]. The high piezoelectric response for the 50-50 vol. % samples could be attributed to their final grain size uniformity that led to a reduction of the 90° domain walls widths improving their mobility to an external stimulus. The origin of the high piezoelectric results for the 50-50 vol. % samples still need further experimentation, including measurements of the domain width, which will be considered in future research effort.

Figure 4.12 shows the dielectric relative permittivity of the 3D printed and pressed disk measured at 1 kHz. Similarly, to piezoelectric properties, the monodispersed samples with small powder particles had a higher dielectric relative permittivity (εr ~ 2391.6 3D printed and εr ~ 3022.9 pressed bodies) compared with the samples with large powder particles (εr ~ 1560.2 3D printed and εr ~ 1858 pressed bodies). A similar tendency was observed in the permittivity for the 3D printed samples in a frequency range from 100 Hz to 1 MHz. While the 50-50 vol. % samples showed the highest dielectric relative permittivity of 2527.5 for 3D printed samples at 1 kHz the pressed samples showed an increase for 50-50 vol. % (εr ~ 2576) and 60-40 vol. % (εr ~ 2639.1). The difference in dielectric permittivity could be attributed to the points previously discussed. However, the increase in dielectric permittivity could be also be affected by carbon residuals from the binder burnout trapped in the microstructure during sintering.

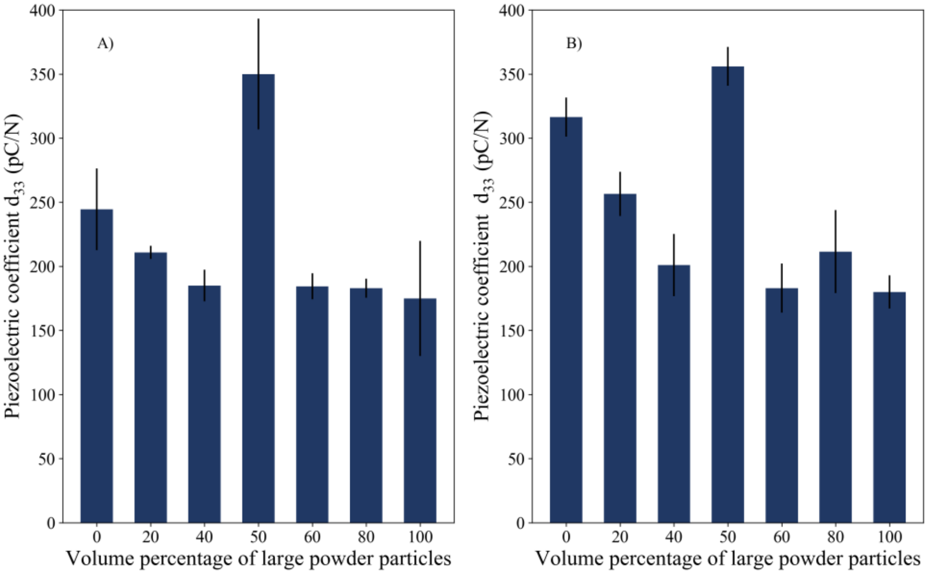

Figure 4.11: Piezoelectric coefficient (d33) after poling for a) 3D printed samples b) Pressed samples.

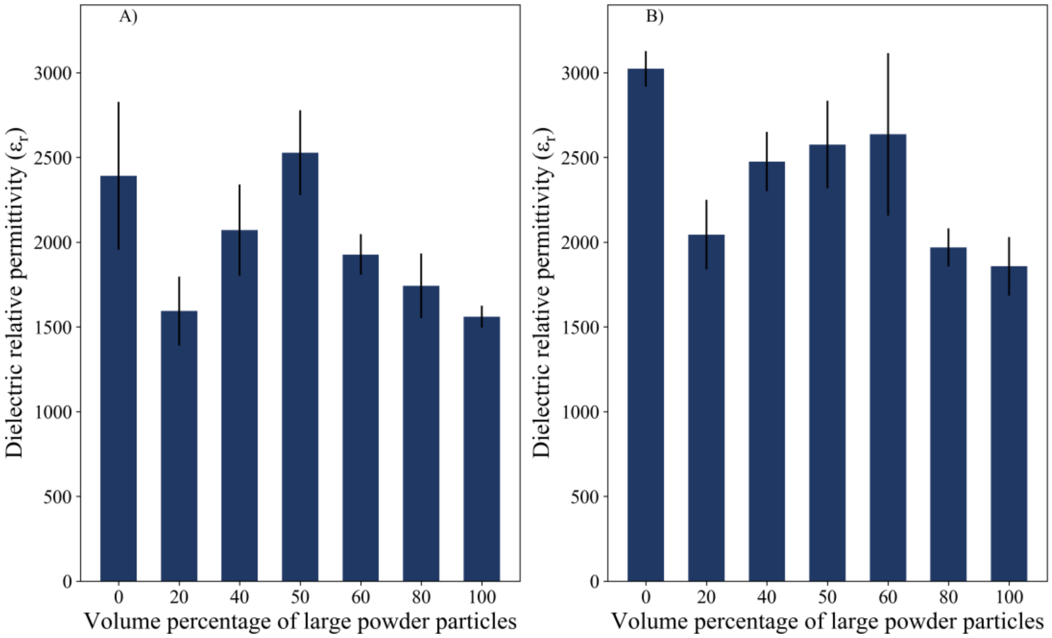

Figure 4.12: Dielectric relative permittivity at 1 kHz. A) 3D printed samples B) Pressed bodies.

3.4 Conclusion

A study to evaluate bimodal particle distribution on BaTiO3 ceramics using PE 3D printing technique was presented. The 3D printed and pressed samples followed a similar behavior in terms of packing density, shrinkage, and piezoelectric properties. It was found that the highest packing density could be obtained using 50-50 % vol. fraction for both types of samples. For the 3D printed samples, a packing density of 35.99 % while for the pressed samples a packing density of 53.62 % could be obtained with respect the theoretical value of BaTiO3. The results on the packing density were verified through the predictive models shown in literature. It was found that the densification rate can be accelerated with the incorporation of small particles leading to highest final density. The shrinkage and density from small monodispersed particles to bimodal mixtures decreased with a different linear behavior depending on the powder size dominant in the mixture, where the apparent inflection point was at 50-50 vol. %. It was found that samples with dominant small particles in the mixture achieve similar properties to the monodispersed samples of 100 nm. Furthermore, bimodal mixtures with large powder particles were found to restricted shrinkage in the samples by relieving some of the stress during sintering. The highest piezoelectric coefficient was obtained with the 50-50% vol. percentage, which is believed to have less variation in the grain growth in the micron level. For the 3D printed samples, using 50-50 vol. % it is possible to obtain a piezoelectric coefficient of 350 pC/N which is 40% higher than the monodispersed sample of 100 nm with 250 pC/N with 15% less density.

References

[1] Advances in Piezoelectric Polymer Composites for Energy Harvesting Applications: A Systematic Review - Mishra - 2019 - Macromolecular Materials and Engineering - Wiley Online Library, (n.d.). https://onlinelibrary.wiley.com/doi/10.1002/mame.201800463 (accessed June 30, 2021).

[2] J. Nonkumwong, P. Sriboriboon, W. Kundhikanjana, L. Srisombat, S. Ananta, Ferroelectric domain evolution in gold nanoparticle-modified perovskite barium titanate ceramics by piezoresponse force microscopy, Integrated Ferroelectrics. 187 (2018) 210–218. https://doi.org/10.1080/10584587.2018.1445350.

[3] I.A. Renteria-Marquez, A. Renteria-Marquez, B.T.L. Tseng, A novel contact model of piezoelectric traveling wave rotary ultrasonic motors with the finite volume method, Ultrasonics. 90 (2018) 5–17. https://doi.org/10.1016/j.ultras.2018.06.004.

[4] H. Kim, A. Renteria-Marquez, M.D. Islam, L.A. Chavez, C.A.G. Rosales, M.A. Ahsan, T.-L.B. Tseng, N.D. Love, Y. Lin, Fabrication of bulk piezoelectric and dielectric BaTiO3 ceramics using paste extrusion 3D printing technique, Journal of the American Ceramic Society. 102 (2019) 3685–3694. https://doi.org/10.1111/jace.16242.

[5] M.D. Maeder, D. Damjanovic, N. Setter, Lead Free Piezoelectric Materials, J Electroceram. 13 (2004) 385–392. https://doi.org/10.1007/s10832-004-5130-y.

[6] T.R. Shrout, S. Zhang, Lead-free piezoelectric ceramics: Alternatives for PZT?, Journal of Electroceramics. 19 (2007). https://doi.org/10.1007/s10832-007-9095-5.

[7] W. Liu, X. Ren, Large Piezoelectric Effect in Pb-Free Ceramics, Phys. Rev. Lett. 103 (2009) 257602. https://doi.org/10.1103/PhysRevLett.103.257602.

[8] Y. Huan, X. Wang, J. Fang, L. Li, Grain Size Effects on Piezoelectric Properties and Domain Structure of BaTiO3 Ceramics Prepared by Two-Step Sintering, Journal of the American Ceramic Society. 96 (2013) 3369–3371. https://doi.org/10.1111/jace.12601.

[9] L.-F. Zhu, B.-P. Zhang, J.-Q. Duan, B.-W. Xun, N. Wang, Y.-C. Tang, G.-L. Zhao, Enhanced piezoelectric and ferroelectric properties of BiFeO3-BaTiO3 lead-free ceramics by optimizing the sintering temperature and dwell time, Journal of the European Ceramic Society. 38 (2018) 3463–3471. https://doi.org/10.1016/j.jeurceramsoc.2018.03.044.

[10] B.P. Conner, G.P. Manogharan, A.N. Martof, L.M. Rodomsky, C.M. Rodomsky, D.C. Jordan, J.W. Limperos, Making sense of 3-D printing: Creating a map of additive manufacturing products and services, Additive Manufacturing. 1–4 (2014) 64–76. https://doi.org/10.1016/j.addma.2014.08.005.

[11] J. Deckers, Additive Manufacturing of Ceramics: A Review, J. Ceram. Sci. Tech. (2014). https://doi.org/10.4416/JCST2014-00032.

[12] T. Huang, M.S. Mason, X. Zhao, G.E. Hilmas, M.C. Leu, Aqueous-based freeze-form extrusion fabrication of alumina components, Rapid Prototyping Journal. 15 (2009) 88–95. https://doi.org/10.1108/13552540910943388.

[13] H. Kim, T. Fernando, M. Li, Y. Lin, T.-L.B. Tseng, Fabrication and characterization of 3D printed BaTiO3/PVDF nanocomposites, Journal of Composite Materials. 52 (2018) 197–206. https://doi.org/10.1177/0021998317704709.

[14] S.M. Gaytan, M.A. Cadena, H. Karim, D. Delfin, Y. Lin, D. Espalin, E. MacDonald, R.B. Wicker, Fabrication of barium titanate by binder jetting additive manufacturing technology, Ceramics International. 41 (2015) 6610–6619. https://doi.org/10.1016/j.ceramint.2015.01.108.

[15] X. Lu, Y. Lee, S. Yang, Y. Hao, J.R.G. Evans, C.G. Parini, Solvent-based paste extrusion solid freeforming, Journal of the European Ceramic Society. 30 (2010) 1–10. https://doi.org/10.1016/j.jeurceramsoc.2009.07.019.

[16] X. Wei, R.S. Nagarajan, E. Peng, J. Xue, J. Wang, J. Ding, Fabrication of YBa2Cu3O7−x (YBCO) superconductor bulk structures by extrusion freeforming, Ceramics International. 42 (2016) 15836–15842. https://doi.org/10.1016/j.ceramint.2016.07.052.

[17] T. Huang, M.S. Mason, G.E. Hilmas, M.C. Leu, Freeze-form extrusion fabrication of ceramic parts, Virtual and Physical Prototyping. 1 (2006) 93–100. https://doi.org/10.1080/17452750600649609.

[18] W. Li, A. Ghazanfari, D. McMillen, M.C. Leu, G.E. Hilmas, J. Watts, Fabricating ceramic components with water dissolvable support structures by the Ceramic On-Demand Extrusion process, CIRP Annals. 66 (2017) 225–228. https://doi.org/10.1016/j.cirp.2017.04.129.

[19] U. Fumio, Y. Hiroshi, N. Kumiko, N. Sachihiko, S. Kenji, M. Yasunori, Swelling and mechanical properties of poly(vinyl alcohol) hydrogels, International Journal of Pharmaceutics. 58 (1990) 135–142. https://doi.org/10.1016/0378-5173(90)90251-X.

[20] A. M'Barki, L. Bocquet, A. Stevenson, Linking Rheology and Printability for Dense and Strong Ceramics by Direct Ink Writing, Scientific Reports. 7 (2017) 6017. https://doi.org/10.1038/s41598-017-06115-0.

[21] T. Hoshina, S. Hatta, H. Takeda, T. Tsurumi, Grain size effect on piezoelectric properties of BaTiO3 ceramics, Jpn. J. Appl. Phys. 57 (2018) 0902BB. https://doi.org/10.7567/JJAP.57.0902BB.

[22] R. Misra, A.J. Barker, J. East, Controlled drying to enhance properties of technical ceramics, Chemical Engineering Journal. 86 (2002) 111–116. https://doi.org/10.1016/S1385-8947(01)00280-7.

[23] C.G. Amza, A. Zapciu, D. Popescu, Paste Extruder—Hardware Add-On for Desktop 3D Printers, Technologies. 5 (2017) 50. https://doi.org/10.3390/technologies5030050.

[24] W.P. Mason, B.T. Matthias, Theoretical Model for Explaining the Ferroelectric Effect in Barium Titanate, Phys. Rev. 74 (1948) 1622–1636. https://doi.org/10.1103/PhysRev.74.1622.

[25] T. Kaully, A. Siegmann, D. Shacham, Rheology of highly filled natural CaCO3 composites. II. Effects of solid loading and particle size distribution on rotational rheometry, Polymer Composites. 28 (2007) 524–533. https://doi.org/10.1002/pc.20309.

[26] H.-W. Gao, R.-J. Yang, J.-Y. He, L. Yang, Rheological behaviors of PVA/H2O solutions of high-polymer concentration, Journal of Applied Polymer Science. 116 (2010) 1459–1466. https://doi.org/10.1002/app.31677.

[27] T. -a. L. Do, J.M. Hargreaves, B. Wolf, J. Hort, J.R. Mitchell, Impact of Particle Size Distribution on Rheological and Textural Properties of Chocolate Models with Reduced Fat Content, Journal of Food Science. 72 (2007) E541–E552. https://doi.org/10.1111/j.1750-3841.2007.00572.x.

[28] C.C. DeMerlis, D.R. Schoneker, Review of the oral toxicity of polyvinyl alcohol (PVA), Food and Chemical Toxicology. 41 (2003) 319–326. https://doi.org/10.1016/S0278-6915(02)00258-2.

[29] B.-K. Yoon, B.-A. Lee, S.-J.L. Kang, Growth behavior of rounded (Ti,W)C and faceted WC grains in a Co matrix during liquid phase sintering, Acta Materialia. 53 (2005) 4677–4685. https://doi.org/10.1016/j.actamat.2005.06.021.

[30] J.-M. Ting, R.Y. Lin, Effect of particle-size distribution on sintering, JOURNAL OF MATERIALS SCIENCE. 29 (1994) 1867–1872. https://doi.org/10.1007/BF00351306.

[31] Y. Wei, Y. Song, X. Deng, B. Han, X. Zhang, Y. Shen, Y. Lin, Dielectric and Ferroelectric Properties of BaTiO3 Nanofibers Prepared via Electrospinning, Journal of Materials Science & Technology. 30 (2014) 743–747. https://doi.org/10.1016/j.jmst.2014.03.021.

[32] H.T. Evans, An X-ray diffraction study of tetragonal barium titanate, Acta Cryst. 14 (1961) 1019–1026. https://doi.org/10.1107/S0365110X61002989.

[33] H.-I. Hsiang, K.-Y. Lin, F.-S. Yen, C.-Y. Hwang, Effects of particle size of BaTiO3 powder on the dielectric properties of BaTiO3/polyvinylidene fluoride composites, Journal of Materials Science. 36 (2001) 3809–3815. https://doi.org/10.1023/A:1017946405447.

[34] M.A. Elqudsy, R.D. Widodo, Rusiyanto, W. Sumbodo, R. Kusumawardani, Megawati, Subiyanto, D. Widjanarko, A. Kusumastuti, The particle and crystallite size analysis of BaTiO3 produced by conventional solid-state reaction process, AIP Conference Proceedings. 1818 (2017) 020012. https://doi.org/10.1063/1.4976876.

[35] A. Renteria, H. Fontes, J.A. Diaz, J.E. Regis, L.A. Chavez, T.-L. (Bill) Tseng, Y. Liu, Y. Lin, Optimization of 3D printing parameters for BaTiO3 piezoelectric ceramics through design of experiments, Mater. Res. Express. 6 (2019) 085706. https://doi.org/10.1088/2053-1591/ab200e.

[36] R. Bjørk, V. Tikare, H.L. Frandsen, N. Pryds, The Effect of Particle Size Distributions on the Microstructural Evolution During Sintering, Journal of the American Ceramic Society. 96 (2013) 103–110. https://doi.org/10.1111/jace.12100.

[37] W. Luan, L. Gao, J. Guo, Size effect on dielectric properties of fine-grained BaTiO3 ceramics, Ceramics International. 25 (1999) 727–729. https://doi.org/10.1016/S0272-8842(99)00009-7.

[38] P. Zheng, J.L. Zhang, Y.Q. Tan, C.L. Wang, Grain-size effects on dielectric and piezoelectric properties of poled BaTiO3 ceramics, Acta Materialia. 60 (2012) 5022–5030. https://doi.org/10.1016/j.actamat.2012.06.015.

[39] M.H. Frey, D.A. Payne, Grain-size effect on structure and phase transformations for barium titanate, Phys. Rev. B. 54 (1996) 3158–3168. https://doi.org/10.1103/PhysRevB.54.3158.

[40] S.K. Robinson, M.R. Paul, Debinding and sintering solutions for metals and ceramics, Metal Powder Report. 56 (2001) 24–34. https://doi.org/10.1016/S0026-0657(01)80324-6.

[41] B.P. Conner, G.P. Manogharan, A.N. Martof, L.M. Rodomsky, C.M. Rodomsky, D.C. Jordan, J.W. Limperos, Making sense of 3-D printing: Creating a map of additive manufacturing products and services, Additive Manufacturing. 1–4 (2014) 64–76. https://doi.org/10.1016/j.addma.2014.08.005.

[42] H. Ogihara, C.A. Randall, S. Trolier-McKinstry, High-Energy Density Capacitors Utilizing 0.7 BaTiO3–0.3 BiScO3 Ceramics, Journal of the American Ceramic Society. 92 (2009) 1719–1724. https://doi.org/10.1111/j.1551-2916.2009.03104.x.

[43] D. Pal, A.K. Chakraborty, S. Sen, S.K. Sen, The synthesis, characterization and sintering of sol-gel derived cordierite ceramics for electronic applications, JOURNAL OF MATERIALS SCIENCE. 31 (1996) 3995–4005. https://doi.org/10.1007/BF00352661.

[44] M.S. Mason, T. Huang, R.G. Landers, M.C. Leu, G.E. Hilmas, Aqueous-based extrusion of high solids loading ceramic pastes: Process modeling and control, Journal of Materials Processing Technology. 209 (2009) 2946–2957. https://doi.org/10.1016/j.jmatprotec.2008.07.004.

[45] S. Zhao, W. Xiao, M.N. Rahaman, D. O'Brien, J.W. Seitz-Sampson, B.S. Bal, Robocasting of silicon nitride with controllable shape and architecture for biomedical applications, International Journal of Applied Ceramic Technology. 14 (2017) 117–127. https://doi.org/10.1111/ijac.12633.

[46] C. Ding, L. Liu, Y. Mei, K.D.T. Ngo, G.-Q. Lu, Magnetic paste as feedstock for additive manufacturing of power magnetics, in: 2018 IEEE Applied Power Electronics Conference and Exposition (APEC), 2018: pp. 615–618. https://doi.org/10.1109/APEC.2018.8341075.

[47] W. Liu, X. Ren, Large Piezoelectric Effect in Pb-Free Ceramics, Phys. Rev. Lett. 103 (2009) 257602. https://doi.org/10.1103/PhysRevLett.103.257602.

[48] H. Chen, Y.F. Zhao, Process parameters optimization for improving surface quality and manufacturing accuracy of binder jetting additive manufacturing process, Rapid Prototyping Journal. 22 (2016) 527–538. https://doi.org/10.1108/RPJ-11-2014-0149.

[49] Y. Wang, Y.F. Zhao, Investigation of Sintering Shrinkage in Binder Jetting Additive Manufacturing Process, Procedia Manufacturing. 10 (2017) 779–790. https://doi.org/10.1016/j.promfg.2017.07.077.

[50] S. Shrestha, G. Manogharan, Optimization of Binder Jetting Using Taguchi Method, JOM. 69 (2017) 491–497. https://doi.org/10.1007/s11837-016-2231-4.

[51] C. Yan, S. Li, L. Yang, L. He, Investigation of FEF process liquid phase migration using orthogonal design of experiments, Rapid Prototyping Journal. 25 (2018) 388–396. https://doi.org/10.1108/RPJ-10-2016-0173.

[52] R. Misra, A.J. Barker, J. East, Controlled drying to enhance properties of technical ceramics, Chemical Engineering Journal. 86 (2002) 111–116. https://doi.org/10.1016/S1385-8947(01)00280-7.

[53] W.P. Mason, B.T. Matthias, Theoretical Model for Explaining the Ferroelectric Effect in Barium Titanate, Phys. Rev. 74 (1948) 1622–1636. https://doi.org/10.1103/PhysRev.74.1622.

[54] J. Ma, L.C. Lim, Effect of particle size distribution on sintering of agglomerate-free submicron alumina powder compacts, Journal of the European Ceramic Society. 22 (2002) 2197–2208. https://doi.org/10.1016/S0955-2219(02)00009-2.

[55] H.-W. Gao, R.-J. Yang, J.-Y. He, L. Yang, Rheological behaviors of PVA/H2O solutions of high-polymer concentration, Journal of Applied Polymer Science. 116 (2010) 1459–1466. https://doi.org/10.1002/app.31677.

[56] A. M’Barki, L. Bocquet, A. Stevenson, Linking Rheology and Printability for Dense and Strong Ceramics by Direct Ink Writing, Sci Rep. 7 (2017) 6017. https://doi.org/10.1038/s41598-017-06115-0.

[57] D. Quemada, Rheology of concentrated disperse systems II. A model for non-newtonian shear viscosity in steady flows, Rheol Acta. 17 (1978) 632–642. https://doi.org/10.1007/BF01522036.

[58] A. Renteria, J.A. Diaz, B. He, I.A. Renteria-Marquez, L.A. Chavez, J.E. Regis, Y. Liu, D. Espalin, T.-L. (Bill) Tseng, Y. Lin, Particle size influence on material properties of BaTiO3 ceramics fabricated using freeze-form extrusion 3D printing, Mater. Res. Express. 6 (2019) 115211. https://doi.org/10.1088/2053-1591/ab4a36.

[59] G.H. Haertling, Ferroelectric Ceramics: History and Technology, Journal of the American Ceramic Society. 82 (1999) 797–818. https://doi.org/10.1111/j.1151-2916.1999.tb01840.x.

[60] I.A. Renteria Marquez, V. Bolborici, A dynamic model of the piezoelectric traveling wave rotary ultrasonic motor stator with the finite volume method, Ultrasonics. 77 (2017) 69–78. https://doi.org/10.1016/j.ultras.2017.01.019.

[61] D.Q. Nguyen, T. Lebey, P. Castelan, V. Bley, M. Boulos, S. Guillemet-Fritsch, C. Combettes, B. Durand, Electrical and Physical Characterization of Bulk Ceramics and Thick Layers of Barium Titanate Manufactured Using Nanopowders, J. of Materi Eng and Perform. 16 (2007) 626–634. https://doi.org/10.1007/s11665-007-9110-7.

[62] J.A. Lewis, Colloidal Processing of Ceramics, Journal of the American Ceramic Society. 83 (2000) 2341–2359. https://doi.org/10.1111/j.1151-2916.2000.tb01560.x.

[63] M. Lanzetta, E. Sachs, Improved surface finish in 3D printing using bimodal powder distribution, Rapid Prototyping Journal. 9 (2003) 157–166. https://doi.org/10.1108/13552540310477463.

[64] R.M. German, Prediction of sintered density for bimodal powder mixtures, Metall Mater Trans A. 23 (1992) 1455–1465. https://doi.org/10.1007/BF02647329.

[65] S. Perko, A. Dakskobler, T. Kosmac, The densification and strength of porous Y-TZP materials with a bimodal particle size distribution for dental applications, Journal of the European Ceramic Society. 32 (2012) 2633–2639. https://doi.org/10.1016/j.jeurceramsoc.2012.02.001.

[66] J.M. Molina, R.A. Saravanan, R. Arpón, C. García-Cordovilla, E. Louis, J. Narciso, Pressure infiltration of liquid aluminium into packed SiC particulate with a bimodal size distribution, Acta Materialia. 50 (2002) 247–257. https://doi.org/10.1016/S1359-6454(01)00348-2.

[67] Y. Shi, Y. Zhang, Simulation of random packing of spherical particles with different size distributions, Appl. Phys. A. 92 (2008) 621–626. https://doi.org/10.1007/s00339-008-4547-6.

[68] D. Sofia, R. Chirone, P. Lettieri, D. Barletta, M. Poletto, Selective laser sintering of ceramic powders with bimodal particle size distribution, Chemical Engineering Research and Design. 136 (2018) 536–547. https://doi.org/10.1016/j.cherd.2018.06.008.

[69] Y. Bai, G. Wagner, C.B. Williams, Effect of Particle Size Distribution on Powder Packing and Sintering in Binder Jetting Additive Manufacturing of Metals, J. Manuf. Sci. Eng. 139 (2017). https://doi.org/10.1115/1.4036640.

[70] W. Du, X. Ren, Y. Chen, C. Ma, M. Radovic, Z. Pei, Model Guided Mixing of Ceramic Powders With Graded Particle Sizes in Binder Jetting Additive Manufacturing, in: American Society of Mechanical Engineers Digital Collection, 2018. https://doi.org/10.1115/MSEC2018-6651.

[71] J.A. Lewis, Direct Ink Writing of 3D Functional Materials, Advanced Functional Materials. 16 (2006) 2193–2204. https://doi.org/10.1002/adfm.200600434.

[72] W. Li, M.C. Leu, Material Extrusion Based Ceramic Additive Manufacturing, 24 (2020). https://doi.org/10.31399/asm.hb.v24.a0006562.

[73] N. Novak, R. Pirc, Z. Kutnjak, Effect of Electric Field on Ferroelectric Phase Transition in BaTiO3 Ferroelectric, Ferroelectrics. 469 (2014) 61–66. https://doi.org/10.1080/15421406.2014.948776.

[74] L.A. Chavez, B.R. Wilburn, P. Ibave, L.C. Delfin, S. Vargas, H. Diaz, C. Fulgentes, A. Renteria, J. Regis, Y. Liu, R.B. Wicker, Y. Lin, Fabrication and characterization of 3D printing induced orthotropic functional ceramics, Smart Mater. Struct. 28 (2019) 125007. https://doi.org/10.1088/1361-665X/ab4e0a.

[75] S. Kumar, O.P. Thakur, V. Luthra, Modulating the Effect of Yttrium Doping on the Structural and Dielectric Properties of Barium Titanate, Physica Status Solidi (a). 215 (2018) 1700710. https://doi.org/10.1002/pssa.201700710.

[76] S.M. Olhero, J.M.F. Ferreira, Influence of particle size distribution on rheology and particle packing of silica-based suspensions, Powder Technology. 139 (2004) 69–75. https://doi.org/10.1016/j.powtec.2003.10.004.

[77] P. D'Haene, J. Mewis, Rheological characterization of bimodal colloidal dispersions, Rheola Acta. 33 (1994) 165–174. https://doi.org/10.1007/BF00437301.

[78] R.M. Turian, T.W. Ma, F.L.G. Hsu, D.J. Sung, Characterization, settling, and rheology of concentrated fine particulate mineral slurries, Powder Technology. 93 (1997) 219–233. https://doi.org/10.1016/S0032-5910(97)03274-9.

[79] B.G. Ravi, R. Chaim, A. Gedanken, Sintering of bimodal alumina powder mixtures with a nanocrystalline component, Nanostructured Materials. 11 (1999) 853–859. https://doi.org/10.1016/S0965-9773(99)00380-3.

[80] B.V. Velamakanni, F.F. Lange, Effect of Interparticle Potentials and Sedimentation on Particle Packing Density of Bimodal Particle Distributions During Pressure Filtration, Journal of the American Ceramic Society. 74 (1991) 166–172. https://doi.org/10.1111/j.1151-2916.1991.tb07313.x.

[81] J.W. Oh, Y. Seong, D.S. Shin, S.J. Park, Investigation and two-stage modeling of sintering behavior of nano/micro-bimodal powders, Powder Technology. 352 (2019) 42–52. https://doi.org/10.1016/j.powtec.2019.04.056.

[82] Y. Shan, J. Xu, G. Wang, X. Sun, G. Liu, J. Xu, J. Li, A fast pressureless sintering method for transparent AlON ceramics by using a bimodal particle size distribution powder, Ceramics International. 41 (2015) 3992–3998. https://doi.org/10.1016/j.ceramint.2014.11.084.

[83] V. Buscaglia, C.A. Randall, Size and scaling effects in barium titanate. An overview, Journal of the European Ceramic Society. 40 (2020) 3744–3758. https://doi.org/10.1016/j.jeurceramsoc.2020.01.021.

[84] J.L. Zhang, P.F. Ji, Y.Q. Wu, X. Zhao, Y.Q. Tan, C.L. Wang, Strong piezoelectricity exhibited by large-grained BaTiO3 ceramics, Appl. Phys. Lett. 104 (2014) 222909. https://doi.org/10.1063/1.4881597.

Vita

Anabel Renteria holds a bachelor degree in Industrial and Systems Engineering with honorable mention from Instituto Tecnoogico de Monterrey Campus Ciudad Juarez. Furthermore, Anabel worked two years for TE Connectivity as Industrial Engineering and one year at 3M Company as a Process Engineer. Later, Anabel obtained her Master of Science in Industrial Engineering from The University of Texas at El Paso. Her thesis "Risk Mitigation in the Supply Chain Caused by Multitple Phase-in and Phase-out Components Using SIMIO Simulation" consisted in the optimization of systems by using discrete events simulations. During her time on the doctoral degree, Anabel holds four first author journal publications and five co-author journal publication, in addition to five working publications.

Contact Information: arenteriamarquez@miners.utep.edu